ICAM

Institute for Computational and Applied Mechanics

BIDIRECTIONAL REFLECTANCE FUNCTIONS FOR APPLICATION TO EARTH RADIATION BUDGET STUDIES

By

N. Manalo-Smith, S. N. Tiwari, and G. L. Smith
Department of Mechanical Engineering
Old Dominion University, Norfolk, VA 23529

NASA Cooperative Agreement NCC1-232 (S. N. Tiwari, P.I.)
NASA Langley Research Center
Hampton, VA 23681-0001

ODU/ICAM Report 97-103
October 1997

BIDIRECTIONAL REFLECTANCE FUNCTIONS FOR APPLICATION TO EARTH RADIATION BUDGET STUDIES

N. Manalo-Smith[1], S. N. Tiwari[2], and G. L. Smith[3]
Old Dominion University, Norfolk, Virginia 23529

ABSTRACT

Reflected solar radiative fluxes emerging for the Earth's top of the atmosphere are inferred from satellite broadband radiance measurements by applying bidirectional reflectance functions (BDRFs) to account for the anisotropy of the radiation field. BDRF's are dependent upon the viewing geometry (i.e. solar zenith angle, view zenith angle, and relative azimuth angle), the amount and type of cloud cover, the condition of the intervening atmosphere, and the reflectance characteristics of the underlying surface. A set of operational Earth Radiation Budget Experiment (ERBE) BDRFs is available which was developed from the Nimbus 7 ERB (Earth Radiation Budget) scanner data for a three-angle grid system. An improved set of bidirectional reflectance is required for mission planning and data analysis of future earth radiation budget instruments, such as the Clouds and Earth's Radiant Energy System (CERES), and for the enhancement of existing radiation budget data products.

This study presents an analytic expression for BDRFs formulated by applying a fit to the ERBE operational model tabulations. A set of model coefficients applicable to any viewing condition is computed for an overcast and a clear sky scene over four geographical surface types: ocean, land, snow, and desert, and partly cloudy scenes over ocean and land. The models are smooth in terms of the directional angles and adhere to the principle of reciprocity, i.e., they are invariant with respect to the interchange of the incoming and outgoing directional angles. The analytic BDRFs and the radiance standard deviations are compared with the operational ERBE models and validated with ERBE data. The clear ocean model is validated with Dlhopolsky's clear ocean model. Dlhopolsky developed a BDRF of higher angular resolution for clear sky ocean from ERBE radiances. Additionally, the effectiveness of the models accounting for anisotropy for various viewing directions is tested with the ERBE alongtract data. An area viewed from nadir and from the side give two different radiance measurements but should yield the same flux when converted by the BDRF. The analytic BDRFs are in very good qualitative agreement with the ERBE models. The overcast scenes exhibit constant retrieved albedo over viewing zenith angles for solar zenith angles less than 60 degrees. The clear ocean model does not produce constant retrieved albedo over viewing zenith angles but gives an improvement over the ERBE operational clear sky ocean BDRF.

[1] Graduate Students, Department of Mechanical Engineering
Old Dominion University, Norfolk, Virginia 23529

[2] Eminent Professor/Scholar, Department of Mechanical Engineering,
Old Dominion University, Norfolk, Virginia 23529

[3] Senior Research Scientist, Atmospheric Sciences Division,
NASA Langley Research Center, Hampton, Virginia 23681-0001

ACKNOWLEDGMENTS

This is a report on the research topic "Earth Radiation Budget Studies." This work was conducted as part of the research activities of the Institute for Computational and Applied Mechanics (ICAM) which is now a subprogram of the Institute for Scientific and Educational Technology (ISET). Within the guidelines of the research project, special attention was directed to "Bidirectional Reflectance Functions for Application to Earth Radiation Budget Studies." The period of performance of the specific research ended December 31, 1996.

The authors would like to extend their sincere appreciation to Drs. S. K. Chaturvedi, R. Dlhopolsky, S. K. Gupta, and W. F. Staylor for their cooperation and helpful discussions during the course of this study. This work, in part, was supported by the NASA Langley Research Center through Cooperative Agreement NCC1-232. The cooperative agreement was monitored by Dr. Samuel E. Massenberg, Director, Office of Education, NASA Langley Research Center, Mail Stop 400.

TABLE OF CONTENTS

Page

ACKNOWLEDGMENTS iii
LIST OF SYMBOLS vi
LIST OF TABLES viii
LIST OF FIGURES ix

Chapter

1. INTRODUCTION 1

2. PHYSICAL PROBLEM AND THEORETICAL FORMULATION 7

2-1. Surface Anisotropy 7
2-2. Bidirectional Reflectance Model 7
2-3. Results from Previous Anisotropy Studies 10
2-3.1. BDRF from Laboratory, Aircraft, TIROS IV and NIMBUS 3 Data 12
2-3.2. BDRF from NIMBUS 7 ERB experiment . . . 13
2-4. ERBE Operational BDRFs 16
2-5. Dlhopolsky BDRF for Clear Ocean Scene 19

3. ANALYTICAL BIDIRECTIONAL REFLECTANCE FUNCTION 23

3 -1. Analytic Form of BDRF for Clear and Partly Cloudy over Ocean 23
3 -2. Analytic Form of BDRF for Land, Snow, Desert, Mostly Cloudy over Ocean and Overcast Scenes . . 27

4. VALIDATION AND RESULTS 33

4-1. Alongtrack Data 33

4-1.1. Alongtrack Scan Experiment 33
4-1.2. Validation of Fluxes with Alongtrack Data . . 36
4-1.3. Presentation of Results 36
4-2. Clear Ocean 40
4-2.1. Clear Ocean (Untuned Analytic Model) 40
4-2.2. Dlhopolsky vs. ERBE Clear Ocean Model . . . 41
4-2.3. Clear Ocean (Tuned) 42
4-3. Overcast 43
4-4. Partly Cloudy Over Ocean 44
4-5. Mostly Cloudy Over Ocean 44

5. CONCLUSIONS 60

REFERENCES 62

APPENDICES 65

A. APPROXIMATION OF SPECULAR ALBEDO FOR CLEAR AND PARTLY CLOUDY OVER OCEAN 66

B. COMPUTATION OF MODEL COEFFICIENTS FOR CLEAR AND PARTLY CLOUDY OVER OCEAN 72

C. COMPUTATION OF MODEL COEFFICIENTS FOR LAND, SNOW, DESERT, MOSTLY CLOUDY OVER OCEAN AND OVERCAST SCENES 76

LIST OF SYMBOLS

a	albedo
ADM	Angular Directional Model
BDRF	Bidirectional Reflectance Function
CERES	Clouds and Earth's Radiant Energy System
Cl	Clear
ERBE	Earth Radiation Budget Experiment
ERBS	Earth Radiation Budget Satellite
GOES	Geostationary Operational Environmental Satellite
L	Radiance
LW	Longwave
M	Flux
MC	Mostly Cloudy
MLE	Maximum Likelihood Estimate
NASA	National Aeronautics and Space Administration
NOAA	National Oceanic and Atmospheric Administration
Ov	Overcast
PC	Partly Cloudy
r	Bidirectional Reflectance
R	Bidirectional Reflectance Function
S	Solar constant
SW	Shortwave
SZA	Solar Zenith Angle
TOA	Top of the Earth's Atmosphere
VZA	Viewing Zenith Angle

Greek Symbols

α	Angle from the line of specular reflection
γ	Scattering angle
ζ	Solar zenith angle
θ	Viewing zenith angle
σ	Standard deviation
ϕ	Relative azimuth angle

Ψ	Azimuthal mean of reflectance

Others

u	$\cos\theta$
u_0	$\cos\zeta$
v	$\sin\theta$
v_0	$\sin\zeta$

LIST OF TABLES

Table		Page
2-1.	ERBE scene types	18
2-2.	Angular bin definitions	22
3-1.	Model coefficients for clear and partly cloudy over ocean	25
3-2.	Model coefficients for land, snow, desert, mostly cloudy over ocean, and overcast scenes	31

LIST OF FIGURES

Figure		Page
1-1.	Radiative interaction in the Earth-atmosphere system	2
2-1.	Geometrical relationship of the sun, satellite and target area	8
2-2.	Schematic of BDRFs for Lambertian and non-Lambertian surfaces	11
2-3.	Taylor and Stowe reflectance pattern for water surface (a) SZA: 0° - 26° (b) SZA: 26° - 37°	14
2-4.	Staylor correlation of bidirectional reflectance with scattering angle for four cloud types	15
2-5.	Staylor and Suttles bidirectional reflectance patterns for clear desert (a) Gibson Desert (b) Saudi Desert	17
2-6.	Maximum likelihood estimate bispectral histogram for clear land	21
3-1.	Correlation of directional reflectance with directional angles (a) Mostly Cloudy over Ocean (b) Overcast	28
3-2.	Model albedo for selected ERBE scene types	32
4-1.	Use of alongtrack data for multiple views of a scene	34
4-2.	Allocation of measurements to alongtrack intervals	35
4-3.	Effect of viewing zenith angle with apparent cloudiness	37
4-4.	Coordinate system used in polar contour diagrams	39
4-5.	Comparison of analytic and ERBE BDRF using nominal model coefficients for clear ocean	

($C_1 = 0.01, C_2 = 0.023, C_3 = 0.800, C_4 = 0.0056, C_5 = 1.060$) . . . 45
(a) SZA: 0°-26°
(b) SZA: 26° - 37°
(c) SZA: 37° - 46°
(d) SZA: 46°- 53°
(e) SZA: 53°- 60°
(f) SZA: 60° - 66°
4-6. Comparison of shortwave radiance standard deviations from analytic and ERBE BDRF for clear ocean
($C_1 = 0.01, C_2 = 0.023, C_3 = 0.800, C_4 = 0.0056, C_5 = 1.060$) . . . 46
(a) SZA: 0°- 26°
(b) SZA: 26° - 37°
(c) SZA: 37° - 46°
(d) SZA: 46°- 53°
(e) SZA: 53°- 60°
(f) SZA: 60° - 66°
4-7. Wind speed effects on clear ocean BDRF 47
(a) SZA: 26° - 37°
(b) SZA: 37° - 46°
4-8. Ratio of alongtrack SW flux using the nominal model coefficients, ERBE BDRF and Dlhopolsky BDRF for clear ocean 48
(a) SZA: 0°- 26°
(b) SZA: 26° - 37°
(c) SZA: 37° - 46°
(d) SZA: 46°- 53°
(e) SZA: 53°- 60°
(f) SZA: 60° - 66°
(g) SZA: 66° - 72°
(h) SZA: 72° - 78°
4-9. Comparison of ERBE and Dlhopolsky BDRF for clear ocean . . 49

(a) SZA: 5°- 10°
(b) SZA: 15°- 20°
(c) SZA: 25°- 30°
(d) SZA: 35°- 40°
(e) SZA: 45°- 50°
(f) SZA: 55°- 60°
4-10. Comparison of analytic and Dlhopolsky BDRF for clear ocean ($C_1 = 0.005$, $C_2 = 0.027$, $C_3 = 0.900$, $C_4 = 0.008$, $C_5 = 1.100$) . . 50
(a) SZA: 5°- 10°
(b) SZA: 15°- 20°
(c) SZA: 25°- 30°
(d) SZA: 35°- 40°
(e) SZA: 45°- 50°
(f) SZA: 55°- 60°
4-11. Ratio of alongtrack SW flux using the alongtrack-tuned model coefficients, ERBE BDRF and Dlhopolsky BDRF for clear ocean 51
(a) SZA: 0°- 26°
(b) SZA: 26°- 37°
(c) SZA: 37°- 46°
(d) SZA: 46°- 53°
(e) SZA: 53°- 60°
(f) SZA: 60°- 66°
(g) SZA: 66°- 72°
(h) SZA: 72°- 78°
4-12. Correlation of analytic BDRF for overcast scene and scattering angle 52
4-13. Comparison of analytic and ERBE BDRF for overcast scene ($A = 0.024$, $B = 1.530$, $G = 0.500$, $K = 0.625$, $\omega = 0.667$) 53
(a) SZA: 0°- 26°
(b) SZA: 26°- 37°

(c) SZA: 37° - 46°
(d) SZA: 46°- 53°
(e) SZA: 53°- 60°
(f) SZA: 60° - 66°
4-14. Comparison of shortwave radiance standard deviations from analytic and ERBE BDRF for overcast scene (A = 0.024, B = 1.530, G = 0.550, K=0.625) 54
(a) SZA: 0°- 26°
(b) SZA: 26° - 37°
(c) SZA: 37° - 46°
(d) SZA: 46°- 53°
(e) SZA: 53°- 60°
(f) SZA: 60° - 66°
4-15. Ratio of alongtrack SW flux using the analytic and ERBE BDRF for overcast scene 55
(a) SZA: 0°- 26°
(b) SZA: 26° - 37°
(c) SZA: 37° - 46°
(d) SZA: 46°- 53°
(e) SZA: 53°- 60°
(f) SZA: 60° - 66°
(g) SZA: 66° - 72°
(h) SZA: 72° - 78°
4-16. Comparison of analytic and ERBE BDRF for partly cloudy over ocean (C_1 = 0.040, C_2 = 0.047, C_3 = 0.577, C_4 = 0.008, C_5 = 1.157) . . 56
(a) SZA: 0°- 26°
(b) SZA: 26° - 37°
(c) SZA: 37° - 46°
(d) SZA: 46°- 53°
(e) SZA: 53°- 60°

(f) SZA: 60° - 66°

4-17. Ratio of alongtrack SW flux for partly cloudy over ocean . . . 57

(a) SZA: 0°- 26°

(b) SZA: 26° - 37°

(c) SZA: 37° - 46°

(d) SZA: 46°- 53°

(e) SZA: 53°- 60°

(f) SZA: 60° - 66°

(g) SZA: 66° - 72°

(h) SZA: 72° - 78°

4-18. Comparison of analytic and ERBE BDRFs for mostly cloudy over ocean (A = 0.025, B = 0.812, G = 0.5250, K = 0.988) 58

(a) SZA: 0°- 26°

(b) SZA: 26° - 37°

(c) SZA: 37° - 46°

(d) SZA: 46°- 53°

(e) SZA: 53°- 60°

(f) SZA: 60° - 66°

4-19. Ratio of alongtrack SW flux using the analytic and ERBE BDRF for mostly cloudy over ocean 59

(a) SZA: 0°- 26°

(b) SZA: 26° - 37°

(c) SZA: 37° - 46°

(d) SZA: 46°- 53°

(e) SZA: 53°- 60°

(f) SZA: 60° - 66°

(g) SZA: 66° - 72°

(h) SZA: 72° - 78°

Chapter 1
INTRODUCTION

In order to enhance our understanding of the radiative energy interaction between the Earth and space, the components of the Earth's radiation budget need to be examined. The availability of remotely-sensed radiance measurements from earth-orbiting and geostationary satellites makes this investigation feasible. The components of the radiation budget are the incident solar flux, the Earth's emitted (longwave) radiation, and the Earth's reflected (shortwave) solar radiation at the top of the atmosphere (TOA), which is considered to be the surface of reference (Fig. 1-1). The TOA longwave (LW) and shortwave (SW) fluxes are not directly measurable quantities, but rather need to be derived from the observed radiances. The radiation emerging from the TOA has an anisotropic distribution and is influenced by the reflectance characteristics of the underlying surface, the illumination and viewing conditions, the optical properties of the intervening atmosphere, and the amount of cloud coverage within the target area [1,2]. The radiance to TOA flux conversion requires knowledge of the angular characteristic of the outgoing radiation field described by angular distribution models (ADMs) or bidirectional reflectance functions (BDRFs), the latter being the term used in this study. These BDRFs account for the dependence of spacecraft-measured radiances on the viewing geometry. Uncertainties in these models lead to errors in the derived net fluxes at TOA, thus describing the Earth radiation budget inaccurately.

Extensive studies of the anisotropic reflectance characteristics for various surface types have been performed using instrumentation on balloons, high-altitude aircraft and on satellites. Earlier assumptions of an isotropic solar radiation, corresponding to a Lambertian Earth surface, resulted in significant errors in the computation of the reflected fluxes [3,4]. Larsen and Barkstrom [5] determined, for

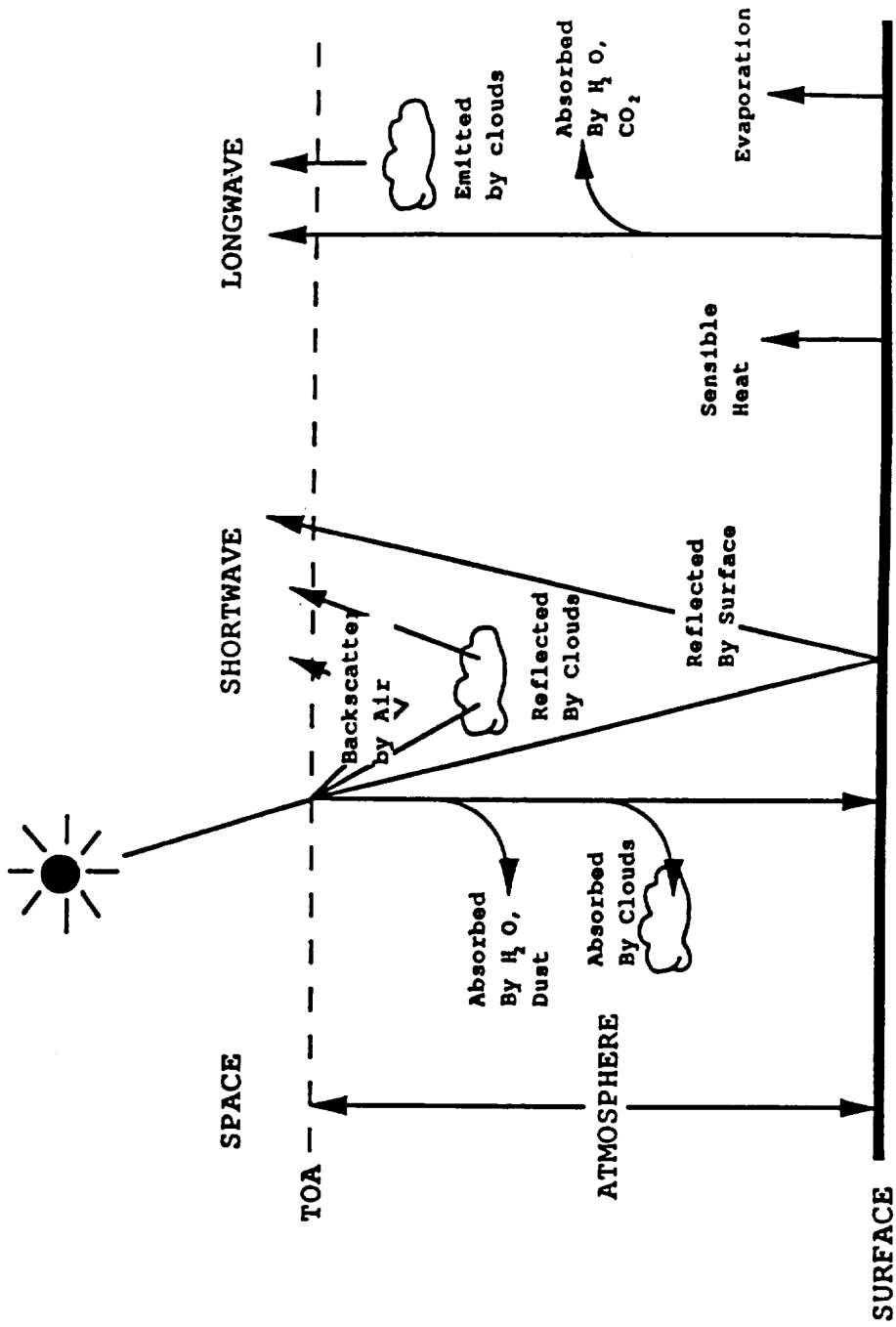

Figure 1-1. Radiative interaction in the Earth-atmosphere system.

instance, that for Arctic latitudes, assumptions of an isotropic surface causes the global albedo to be overestimated. Coulson and Reynolds [6] used laboratory-gathered bidirectional reflectance data to describe the anisotropic properties for various land surfaces, discriminated by soil and vegetation type. Brennan and Bandeen [7] used a medium resolution infrared radiometer (MRIR) aboard the National Aeronautics and Space Administration's (NASA) Convair-990 high-altitude research aircraft to investigate the anisotropic patterns of clouds, water and land surfaces. Salomonson and Marlatt [8] studied the anisotropic characteristics of three highly reflective surfaces, namely stratus clouds, snow and white gypsum sand, from data collected using the NIMBUS F3 MRIR mounted on a Piper Twin Comanche aircraft with a flight altitude ceiling of 9000 meters.

Because satellites provide more comprehensive spatial and temporal coverage over the entire earth, satellite measurements are ideal for developing anisotropic models. Moreover, since measurements are made above the atmosphere, more realistic determination of the incoming and outgoing radiation is possible. Additionally, surfaces can be viewed from a larger range of illumination and viewing directions. Ruff et al. [9] studied the angular properties of clouds from radiometric measurements aboard the TIROS IV spacecraft. Although relatively high resolution radiometers were deployed on the TIROS satellite series and on NIMBUS 2, the need to obtain data that complied with spatial resolution requirements over an extended period of time was not met until the deployment of the NIMBUS 3 spacecraft. This mission provided the opportunity to study the annual global budget over a continuous period for the first time [2]. Bidirectional reflectance models for three surface types (ocean, cloud-land, snow) were applied for three solar zenith angle ranges.

The first scanning instruments designed specifically to measure the radiation budget flew aboard the NIMBUS 6 and 7 satellites [10,11]. The NIMBUS 7

satellite was launched in October 1978 into a noon (ascending node) sunsynchronous orbit at an altitude of 950 km. The NIMBUS 7 Earth Radiation Budget (ERB) scanning instrument was equipped with a biaxially scanning set of eight optical telescopes, four of which monitored broadband SW (0.2 - 4.0 μm) radiation and the remaining four monitoring broadband LW (4.0 - 50 μm) radiation. The spatial resolution varied from 90 km x 90 km at nadir to 250 km x 250 km at a maximum scan angle of 72° [11]. The operational scan modes of the radiometers permitted radiance observations in the principal plane of the sun where the angular variations of the reflected sunlight are most prominent. This instrument was designed to yield data necessary for the development of a comprehensive set of BDRFs. However, orbit configuration and scanning constraints have inhibited a more complete angular coverage. The scanning instruments on the NIMBUS 6 and 7 satellites have provided extensive datasets from which anisotropic models have been developed. Taylor and Stowe [12] developed bidirectional models for eight uniform surface types from the NIMBUS 7 measurements. Staylor [13] and Staylor and Suttles [14] developed BDRFs for clouds and deserts, respectively, using NIMBUS 7 scanner measurements. The present models used to process data from the Earth Radiation Budget Experiment (ERBE) [15] were derived from the NIMBUS 7 Earth Radiation Budget (ERB) and the Geostationary Operational Environmental Satellite (GOES) data sets [16].

Some uncertainties in early earth radiation budget measurements are attributed to poor temporal coverage by a single, sunsynchronous spacecraft. The issue of poor diurnal sampling was addressed with the inception of ERBE, a multiple satellite mission. The orbital configuration of the multi-satellite system allowed for adequate temporal and spatial coverage. ERBE consists of three spacecrafts, the Earth Radiation Budget Satellite (ERBS), and the NOAA-9 and NOAA-10 spacecrafts. ERBS is a ERBE-dedicated spacecraft that was launched into orbit in

October 1984 in a 57° inclination orbit with an altitude of 600 km, restricting latitudinal coverage between 57°N and 57°S. The NOAA-9 and NOAA-10 are high altitude sunsynchronous satellites deployed to altitudes of 812 km and 830 km, respectively. The ERBS has a westward precessional period of 72 days around the earth while the NOAA-9 and NOAA-10 have equator crossing times of 1430 (ascending node) and 0730 (descending node), respectively. The ERBE scanning package consists of a shortwave (0.2 - 5.0 μm), a longwave (5 - 50 μm), and a total (0.2 - 50 μm) radiometer. The radiometers, sweeping from horizon to horizon, are mounted on a single scan head and boresighted [17] so as to detect radiation from the same field of view. The normal operating mode is in the cross-track scan direction; although, for limited periods in 1985 (January and August), the scanner was rotated 90° in azimuth to operate in the alongtrack scan mode. Operation in this mode is ideal for determining LW limb-darkening functions [18,19] and for validating shortwave anisotropic models because it allows for a single site on the satellite ground track to be viewed from different viewing zenith angles during a single orbital pass.

Dlhopolsky [20] utilized ERBE shortwave radiance measurements to generate an improved set of angular directional models with increased angular resolution for clear sky over ocean surface.

The accuracy of future radiation budget data products can be enhanced with an improved set of BDRFs. The improved set of BDRFs must be continuous and smooth from one angular bin to another. It must also satisfy reciprocity (i.e. interchanging the incident and reflected directions must yield the same flux contribution). Additionally, radiances that are measured from different viewing angles over a single site must be converted to the same flux if the bidirectional reflectance function is modeled correctly (i.e. there is no albedo growth from nadir to limb). The present ERBE operational models are discontinuous from one bin to

another and do not satisfy reciprocity. Moreover, there is about a 10% albedo growth from nadir to limb.

The objective of this study is to develop an analytic BDRF that shows the dependence of the solar reflected radiation on surface, cloud, viewing geometry, and atmospheric conditions. This study presents a simple analytic formulation of the BDRFs to model the anisotropy of nine of the twelve ERBE scene types. The nine basic scene types are classified according to geographical surface type (ocean, land, snow, desert) under varying degrees of cloud cover (clear, partly cloudy, mostly cloudy, overcast). The remaining three scenes are mixed scenes that are assumed to be made up of 50% ocean and 50% land (e.g. coast). The model coefficients are derived by applying an analytic fit to the NIMBUS 7 BDRFs [16] which were used to process ERBE data. For each scene type, a single set of model parameters is required for application to any combination of viewing geometries. This analytic formulation satisfies the principle of reciprocity and avoids the discontinuity from one discrete angular bin to another as observed from the ERBE operational BDRFs. The analytic BDRFs are validated by comparison of the resulting radiances and TOA fluxes with ERBE observations. Model results and validation thereof are presented for clear, partly cloudy, mostly cloudy over ocean and overcast scenes. Results of this study will be used for mission-planning and data interpretation of next-generation earth radiation budget programs such as the Clouds and Earth's Radiant Energy System (CERES) mission [21].

The physical problem and theoretical formulation are presented in Chap. 2. The analytic form of the BDRF is developed in Chap. 3. Chapter 4 discusses the validation techniques and results. Finally, conclusions that were drawn from this study are presented in Chap. 5.

Chapter 2

PHYSICAL PROBLEM AND THEORETICAL FORMULATION

2-1. Surface Anisotropy

When solar radiation impinges on the Earth-atmosphere system, it is reflected in various directions. The reflected shortwave radiances are dependent upon the direction from which a surface is being viewed as well as on the surface angular reflectance characteristics. Most natural surfaces exhibit varying degrees of reflectance in different directions. A specular surface, such as the ocean surface, is mirror-like in its nature of reflectance and highly direction-dependent, while a diffuse surface will reflect uniformly in all direction. This directional dependence of the radiation field is defined as anisotropy. All Earth surfaces exhibit some degree of reflectance anisotropy which is described by bidirectional reflectance functions (BDRFs). Aside from their dependence on the underlying surface, the BDRFs are also influenced by the amount of cloud cover and the state of the intervening atmosphere.

2-2. Bidirectional Reflectance Model

The reflected radiance L leaving the top of the Earth's atmosphere varies with direction. The geometric relationship used in this study is depicted in Fig. 2-1 [16]. The angle between ray from the sun and the normal to the target area is the solar zenith angle ζ while the angle between zenith ray and the normal to the target area is the viewing zenith angle θ. The relative azimuth angle ϕ is the angular distance of the satellite from the principal plane, i.e. the plane containing the sun, the Earth's center and the point of observation. The azimuth angle for an exiting ray is measured from the principal plane on the side away from the sun. Thus, reflection in the forward direction corresponds to $\phi=0^\circ$ while backward reflection corresponds to $\phi = 180^\circ$. The reflected shortwave flux M is obtained by integrating the radiances L over all the outgoing directions such that

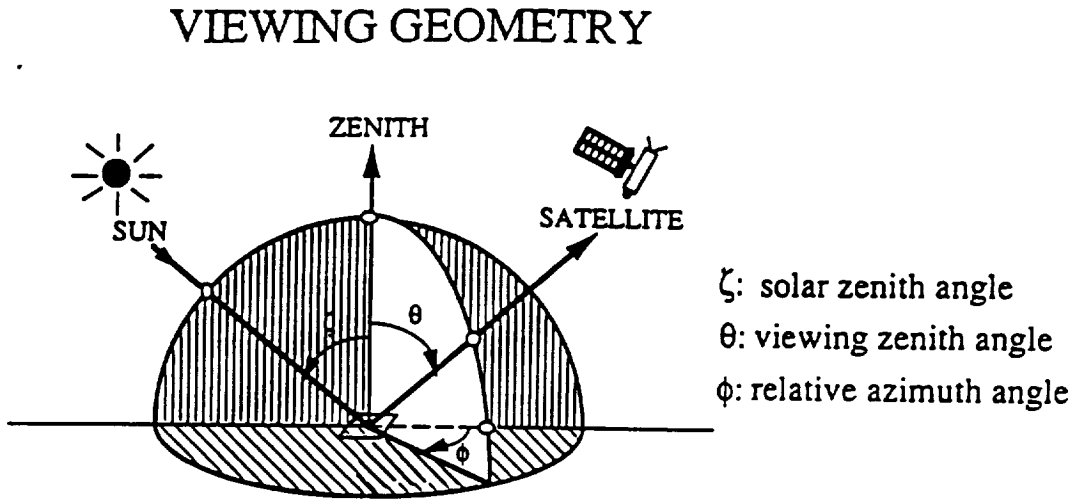

Figure 2-1. Geometrical relationship of the sun, satellite and target area.

$$M = \int_0^{2\pi} \int_0^{\pi/2} L(\theta, \phi, \zeta) \cos\theta \sin\theta d\theta d\phi \tag{2.1}$$

The flux M has units of Wm^{-2} while L has units of $Wm^{-2}\ sr^{-1}$. For an isotropic surface (i.e. the reflected radiation is the same in all directions), $M = \pi L$. The bidirectional reflectance function (BDRF) R , which characterizes the anisotropy of the reflected radiance, is the ratio of Lambertian flux obtained from the observed radiance in a given direction to the actual flux computed by Eq. (2.1) and is given by

$$R(\theta, \phi, \zeta) = \pi L(\theta, \phi, \zeta) / M \tag{2.2}$$

Values of BDRF equal to unity imply a radiance measurement will provide the correct radiant flux assuming isotropy. Any departure from unity corresponds to the fractional error that is incurred if the measured radiance is used to estimate the radiant flux for an isotropic assumption (i.e. BDRF < 1.0 (>1.0) overestimates (underestimates)) the flux by an amount equal to the portion lesser (greater) than unity).

The normalization condition for R is derived by substituting Eq. (2.2) into Eq. (2.1) giving

$$\int_0^{2\pi} \int_0^{\pi/2} R \cos\theta \sin\theta d\theta d\phi = \pi \tag{2.3}$$

The albedo at TOA is defined as

$$M = Sa(\zeta) \cos\zeta \tag{2.4}$$

where S is the solar flux, a is the albedo at TOA and ζ is the solar zenith angle.

The reflected radiation adheres to the principle of reciprocity [22]. This principle states that for a given observation point, the positions of the spacecraft and

sun may be interchanged and still yield the same flux contribution. From this principle, it follows that

$$R(\theta, \phi, \zeta)\, a(\zeta) = R(\zeta, \phi, \theta)\, a(\theta) \tag{2.5}$$

The quantity $r(\theta, \phi, \zeta) = R(\theta, \phi, \zeta)\, a(\zeta)$ is called the bidirectional reflectance.

The BDRFs are dependent upon the underlying geographical type (ocean, land, snow, desert, coast), the cloud cover (i.e. clear, partly cloudy, mostly cloudy and overcast), and the viewing geometry (sun, spacecraft, and observation point geometry). Perturbations in the atmospheric conditions also strongly influence anisotropy (e.g. nature of scattering particles, turbidity). Figure 2-2 is a schematic illustration of BDRFs for a Lambertian surface and two variations which are non-Lambertian. Fluxes retrieved by using each of these will be different. It illustrates that the use of the wrong BDRF will result in errors in retrieved fluxes. The directional models that are presently being used to process data from earth radiation missions, such as the ERBE, are not closely approximated by a Lambertian model. The dotted line is a more realistic representation of the anisotropy of the radiation field for most scene types in which the atmospheric perturbations that causes these models to deviate from the mean values are considered. This diagram shows that the set of operational models used to process earth radiation budget data is a more realistic representation of anisotropy than a Lambertian surface assumption.

2-3. Results from Previous Anisotropy Studies

Studies to determine the anisotropic patterns of the outgoing radiation field from various surface types have been performed using balloon, aircraft and satellite data. A few studies have been selected and their results presented in the following sections. The first section briefly discusses results from aircraft, laboratory, and satellite (TIROS IV and NIMBUS 3) experiments. The second section describes the BDRFs generated from the NIMBUS 7 data. Finally, the third

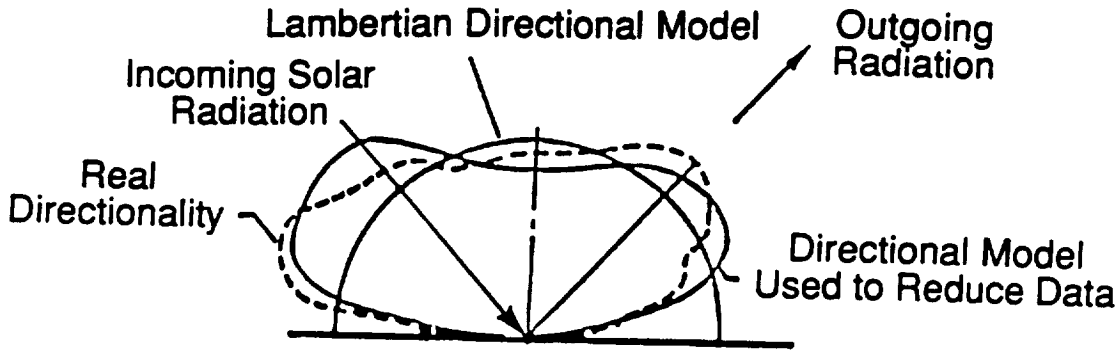

Figure 2-2. Schematic of BDRFs for Lambertian and non-Lambertian surfaces.

section introduces the Dlhopolsky BDRF for clear ocean that were developed from ERBE radiances.

2-3.1. BDRF from Laboratory, Aircraft and TIROS IV and NIMBUS 3 Data

Coulson et al. [23] conducted laboratory experiments on the anisotropic characteristics of natural sands and soils, particularly red clay soil and white quartz sand. These surfaces were found to exhibit a more pronounced reflectance in the backward scatter direction than in the forward scatter region. No increase in anisotropy in the specular direction was observed. Furthermore, an increase in reflectance occurred as the solar zenith angle increased.

Meanwhile, using a NIMBUS F3 medium resolution radiometer aboard a Piper Twin Comanche aircraft, Salomonson and Marlatt [8] determined the anisotropic patterns for snow, white sand, and stratus clouds. Stratus clouds were found to be more anisotropic than the other two surfaces. These clouds were significantly more anisotropic in the backscatter direction than in the forward scatter direction. Snow had higher reflectances in the forward scatter region, most notably in the specular reflection region while white sand was more of a back-reflecting surface. For the three surface types, an increase in anisotropy accompanied an increase in incident angle.

Ruff et al. [9] studied the cloud anisotropic properties from TIROS IV meteorological satellite data. This study showed clouds are primarily forward reflecting. Again, a marked increase in anisotropy was observed as the solar zenith angle increased.

The deployment of a five-channel scanning radiometer aboard the NIMBUS 3 spacecraft presented the first opportunity to study the earth's radiation budget with high resolution data [2]. NIMBUS 3 was launched on April 14, 1969 into a retrograde, sunsynchronous, nearly circular polar orbit. Equator crossing times were 1130 (northbound) and 2330 (southbound). In order to evaluate the satellite

data, a set of empirical reflectance models obtained from various sources, including Salomonson and Marlatt [8] and Ruff et al. [9] results, was applied to three scene type classifications for three solar zenith angle ranges. The models characterized the anisotropy of clear ocean, high latitude ice and snow, and cloud and land (cloud-land) for 0°- 35°, 35° - 60°, and 60° - 80° solar zenith angle ranges. The cloud-land model exhibited limb-brightening in the backward scatter region($60° < \zeta < 80°$) and was nearly isotropic in the same region for $35° < \zeta < 60°$. The cloud-free ocean showed an increase in anisotropy with increasing incident angle.

2-3.2. BDRF from NIMBUS 7 ERB Experiment

Bidirectional reflectance functions using broadband observations from NIMBUS 7 Earth radiation budget (ERB) data have been developed for a number of scene types [12-14,16]. Taylor and Stowe [12] constructed BDRFs from Nimbus 7 data for eight uniform surface types (land, water, snow, ice, low, middle, high water and ice clouds) covering a period of 61 days over regions approximately 160 km x 160 km, called "sub-target areas". From the dataset used over the time period covered for their study, these authors determined that only 3% of the bins were unsampled and thus required interpolation. Results included anisotropic patterns, SWR standard deviations, and relative dispersion, which measures the variability of radiance within the bin. All surfaces studied exhibited an increase in specularity with increasing solar zenith angles, similarity in the anisotropy of high water and ice clouds, high backscatter for land surfaces for large solar zenith angles, and limb-brightening for water surfaces. Figure 2-3 [12] show the bidirectional reflectance pattern for ocean surface for SZA range 0°-26° (Fig. 2-3a) on the left portion of the contour plot, and for SZA 26°-37° (Fig. 2-3b) on the right half. These plots illustrate the presence of the sun glint region and its shift towards the limb as the sun moves.

The anisotropic modeling of clouds [13] and deserts [14] utilized a reflectance model consisting of the sum and product terms of the cosines of the solar and viewing zenith angles, thus establishing reciprocity between these angles.

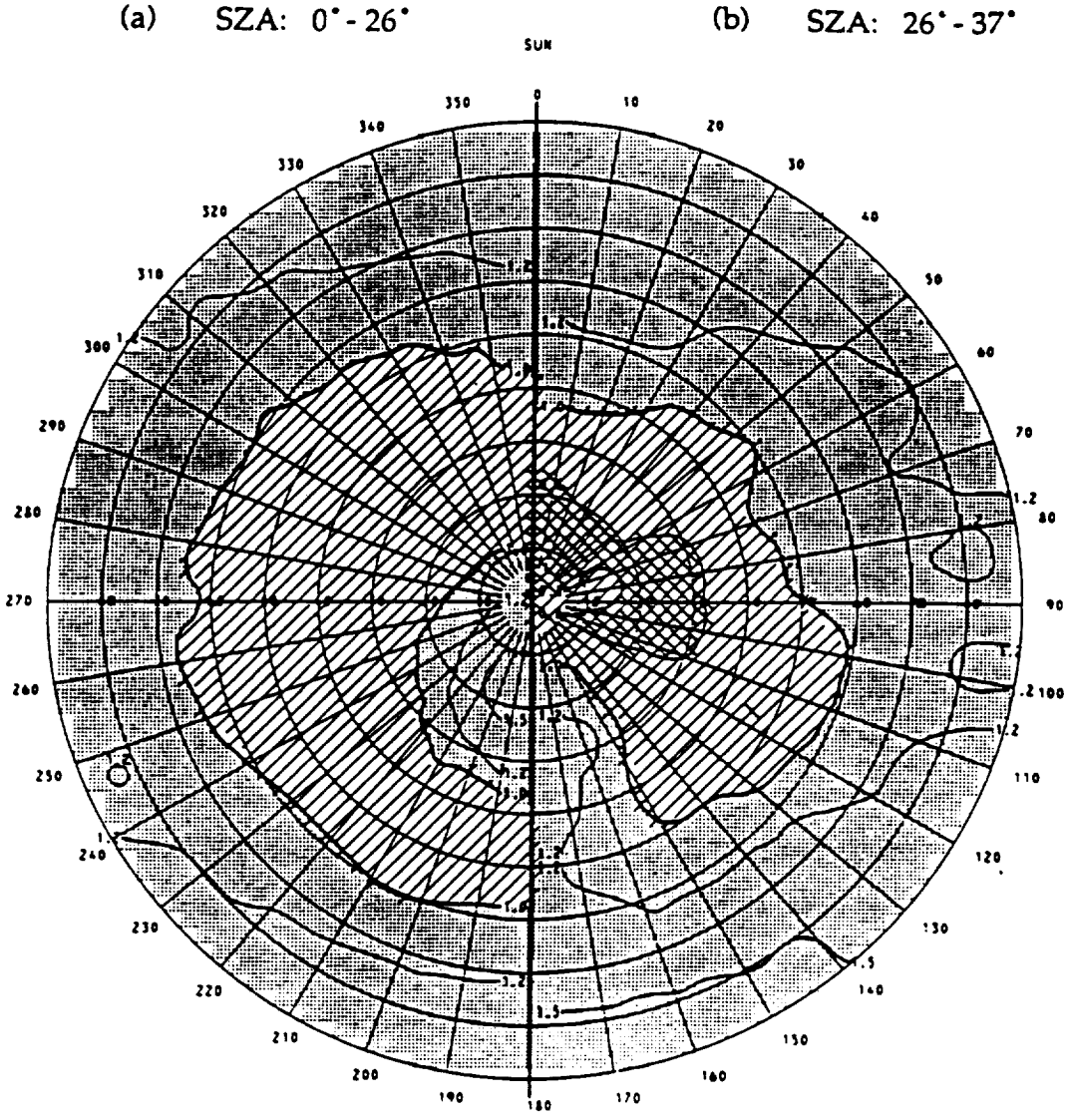

Figure 2-3. Taylor and Stowe reflectance pattern for water surface.

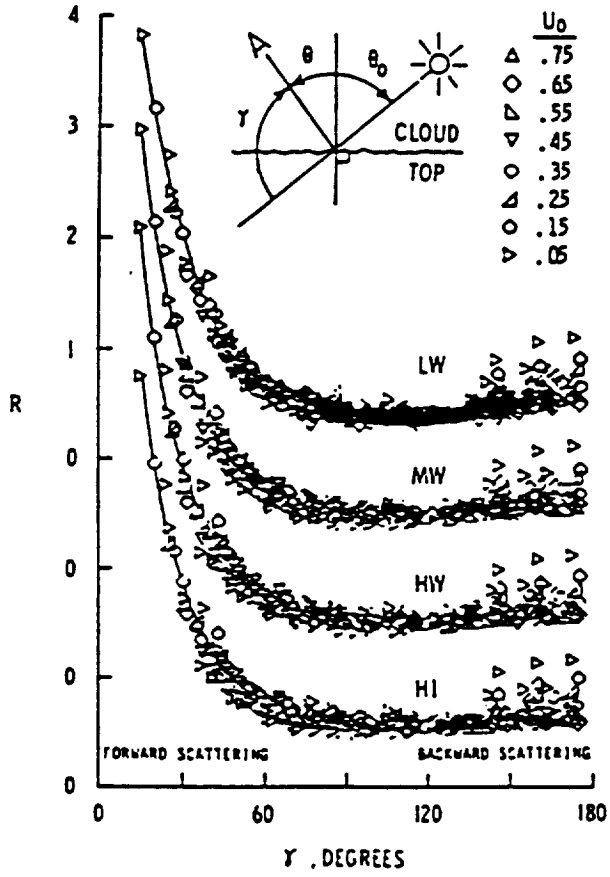

Figure 2-4. Staylor correlation of bidirectional reflectance with scattering angle for four cloud types.

Bidirectional reflectance patterns as a function of the scattering angle for four cloud types (low water, middle water, high water, high ice clouds) exhibit strong forward scatter peaks (Fig. 2-4). The correlation of the bidirectional reflectance with the scattering angle for the four cloud categories do not show significant differences in the shape of correlation.

Staylor and Suttles [14] and Staylor [24] applied an analytic fit to the NIMBUS 7 radiance observations to generate BDRF for desert surfaces under a clear sky condition. The target sites selected were the Sahara desert, the Gibson desert, and Saudi desert. The Sahara desert has little vegetation and moisture and has expansive sand dunes and sand seas. The Gibson desert, located in Western Australia is characterized by a mix of sand dunes, rock outcropping and arid steppe vegetation. The Saudi desert site is characterized by sand dunes and sand seas with no vegetation. Bidirectional reflectance patterns for the Gibson and Saudi deserts (Fig. 2-5) indicate that this surface type is primarily a back-reflector. Results also show that deserts exhibit varying degrees of anisotropy (e.g. Saudi desert is more nearly-isotropic than either Gibson or Sahara deserts).

2-4. ERBE Operational BDRFs

Suttles et al. [16] analyzed the NIMBUS 7 and GOES (November 1978) instrument data. The geosynchronous spacecraft GOES was positioned at 75°W and made observations between 135°W and 15°W longitudinally and 60°N and 60°S latitudinally. The GOES radiometers detected radiances in the narrowband spectral intervals. These narrowband measurements were converted to broadband radiances and combined with the NIMBUS 7 ERB measurements to generate BDRFs for 12 homogeneous Earth and cloud surfaces. A model exists for clear (0-5%), partly cloud (5-50%), mostly cloudy (50-95%), and overcast (95-100%) scenes over ocean, land, coast, snow and desert. A single overcast composite model is used that incorporates the features of the overcast over ocean and overcast over land scenes. The complete set of ERBE scene types are tabulated on Table 2-1. The surface type is first determined by referring to a static geographical

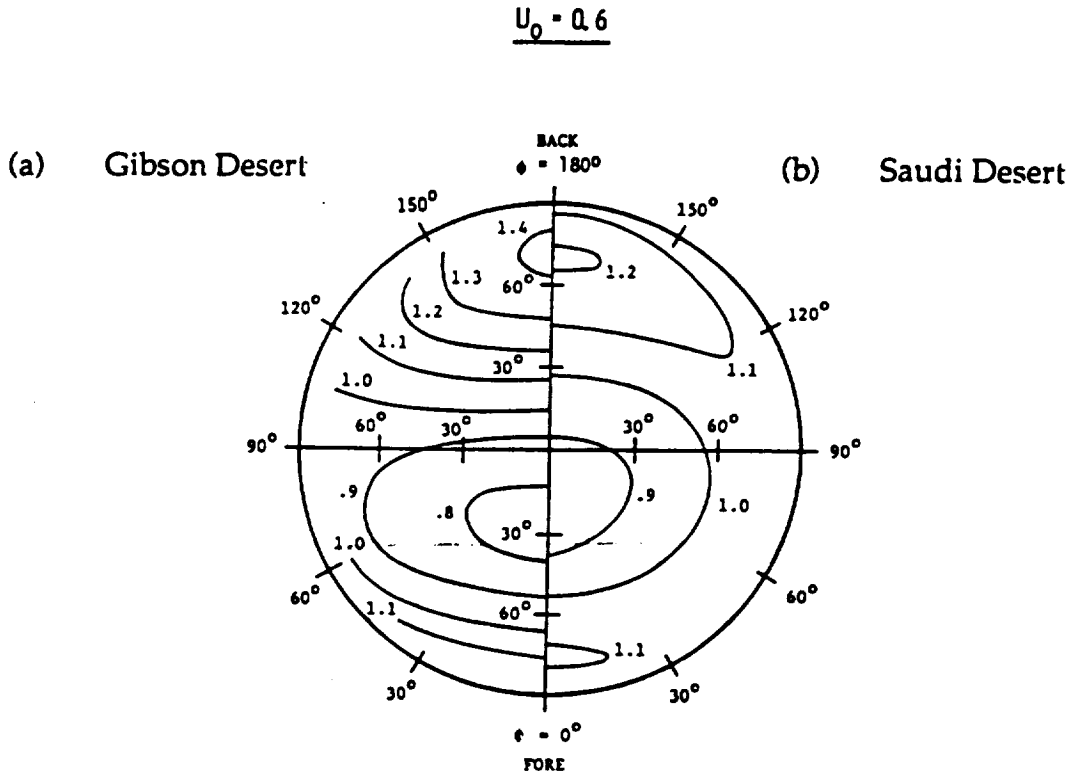

Figure 2-5. Staylor and Suttles bidirectional reflectance patterns for clear desert.

Table 2-1. ERBE scene types

	Scene	Cloud Cover (%)
1	Clear over Ocean	0 - 5
2	Clear over Land	0 - 5
3	Clear over Snow	0 - 5
4	Clear over Desert	0 - 5
5	Clear over Coast	0 - 5
6	PC over Ocean*	5 - 50
7	PC over Land	5 - 50
8	PC over Coast	5 - 50
9	MC over Ocean**	50 - 95
10	MC over Land	50 - 95
11	MC over Coast	50 - 95
12	Overcast	95 - 100

* PC - Partly Cloudy
** MC - Mostly Cloudy

map while the cloud cover category was identified by a Maximum Likelihood Estimate (MLE) technique [25]. The MLE technique uses a bispectral cloud fraction identification technique that uses simultaneously measured shortwave and longwave radiances. Figure 2-6 illustrates, for a given geographical surface type and viewing geometry, an example of a bispectral radiance histogram that groups measurement pairs into four cloud categories. Associated with each cloud class is a mean radiance and other a priori information and statistics that are used to evaluate the probability of a measured pair belonging to one of the four cloud types. The cloud category which has the highest probability of occurrence is the cloud class selected. The bidirectional parameters (BDRFs, standard deviations of mean shortwave radiances, and shortwave-longwave radiance correlation coefficients) are tabulated in discrete angular bins, defined for angular ranges of ζ, θ and ϕ to provide discrete values for modeling and presentation. Table 2-2 lists the angular bins used by Suttles et al. [16]. Sparsely sampled or unsampled angular bins were filled with models estimated by applying reciprocity, interpolation or extrapolation techniques.

With the exception of snow scene type, the anisotropic patterns of the ERBE scene types show notable limb-brightening at high solar zenith angles. Ocean surfaces demonstrate significant specular reflection in the region of forward scattering for $\zeta = 0 - 45^{\circ}$. The models increase in anisotropy with increasing viewing zenith angles. Clear snow is limb-darkened for $\zeta < 53^{\circ}$.

These angular models are presently being used in the inversion of satellite radiance measurements from ERBE satellites to fluxes at TOA.

2-5. Dlhopolsky BDRF for Clear Ocean Scene

Dlhopolsky [20] investigated the effects of higher angular resolution on the instantaneous albedos for clear sky over ocean scenes. The effects of ocean surface roughness on BDRF due to the effects of wind speed are also discussed in this study. Dlhopolsky has found that the reflected radiation is higher for a higher wind speed since the wave slope causes the incident angle to be larger.

Meanwhile, a calm surface reflects a significant amount of energy in the direction of forward scatter. In formulating BDRFs from ERBS data, she processed ERBS clear sky data for the months of April 1985 through November 1985 to generate a reflectance matrix sorted into 5°x5°x5° discrete angular bins. This resolution is a significant refinement compared to the first solar zenith angle bin used by Suttles et al.[10] which covered 0° - 26° incident zenith angles. The Dlhopolsky study determined that the NIMBUS 7 angular bin size was not adequate for estimating the anisotropy in this bin range. The BDRFs for the first ERBE solar zenith angle bin in particular, which ranges from 0° - 26°, generally overestimated the instantaneous albedos. Reflectances are also better represented in the refined angular bins, especially in the specular directions. Differences in BDRFs between Dlhopolsky and ERBE models are on the order of 10% for nonspecular directions and increases significantly in the specular direction for solar zenith angles less than 35°.

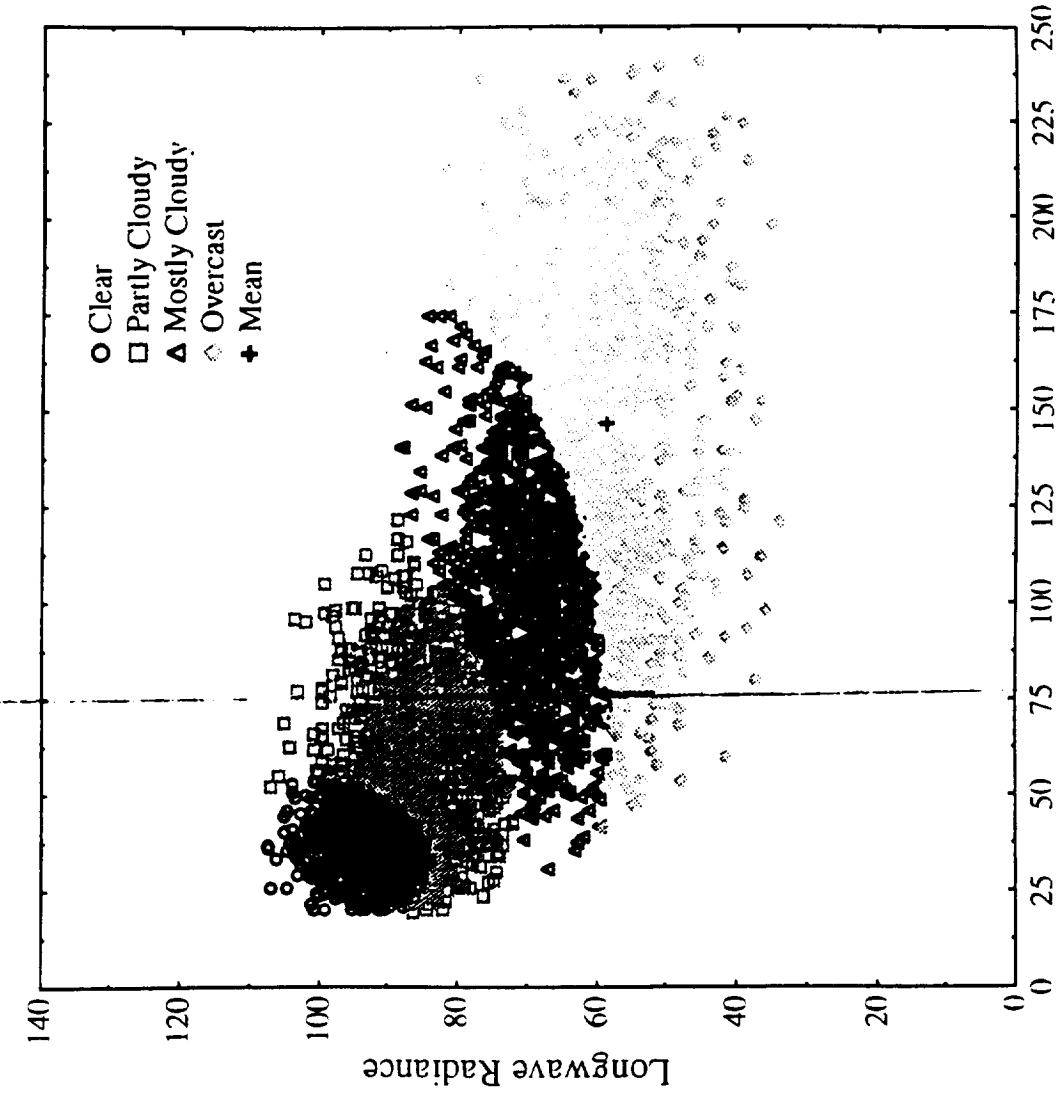

Figure 2-6. Maximum likelihood estimate bispectral histogram for clear land.

Table 2-2. Angular bin definitions

Bin No.	Solar Zenith Angle	Viewing Zenith Angle	Relative Azimuth Angle
1	0.0 - 25.84	0 - 15	0 - 9
2	25.84 - 36.87	15 - 27	9 - 30
3	36.87 - 45.57	27 - 39	30 - 60
4	45.57 - 53.13	39 - 51	60 - 90
5	53.13 - 60.00	51 - 63	90 - 120
6	60.00 - 66.42	63 - 75	120 - 150
7	66.42 - 72.54	75 - 90	150 - 171
8	72.54 - 78.46		171 - 180
9	78.46 - 84.26		
10	84.26 - 90.00		

Chapter 3

ANALYTICAL BIDIRECTIONAL REFLECTANCE FUNCTION

The ERBE operational models tabulated by Suttles et al. [16] can be closely approximated by applying an analytic fit to these tabulation to obtain an empirical form for the bidirectional reflectance. An analytic form of the bidirectional reflectance for clear and partly cloudy over ocean scenes is discussed, followed by an analytic model for the land, snow, desert, mostly cloudy over ocean and overcast ERBE scene types. The forms of these expressions are based on theoretical considerations.

3-1. Analytic Form of BDRF for Clear and Partly Cloudy over Ocean

The bidirectional reflectance for clear and partly cloudy over ocean can be expressed in the following empirical form [26]

$$r_0(\theta, \phi, \zeta) = C_1 + \frac{C_2(1+\cos^2\gamma)}{(uu_0)^{C_3}} + \frac{C_4(C_5 - 1)}{(uu_0)^{1.5}(C_5 - \cos\alpha)^2} \tag{3.1}$$

where $u = \cos\theta$, $u_0 = \cos\zeta$, γ is the scattering angle, i.e. the angle through which the ray is turned as it is reflected, and α is the angle from the line of specular reflection. These angles are defined by $\cos\gamma = vv_0\cos\phi - uu_0$ and $\cos\alpha = vv_0\cos\phi + uu_0$, where $v = \sin\theta$ and $v_0 = \sin\zeta$. The second term on the right-hand side accounts for Rayleigh scattering from the atmosphere and for atmospheric absorption. The Rayleigh phase function is given by $1 + \cos^2\gamma$ and the parameter C_2 is associated with the Rayleigh optical depth. The parameter C_3 accounts for the atmospheric absorption and is affected by the presence of aerosols. This form for atmospheric absorption is used instead of an exponential

term because it is analytically tractable. The last term on the right-hand side accounts for the specular reflection from the ocean surface. When radiation is scattered from a smooth surface, such as the calm ocean, there is a sharp peak in the forward scatter direction. The form of the specular term was determined by fitting the ERBE operational models choosing an even function in terms of the specular angle, α, which leads to the term $(C_5 - \cos\alpha)$. With high winds, the waves over the ocean will cause the forward scattering peak to broaden while for calm conditions, the ocean surface will be flat thus causing the reflection to be sharply peaked. The first term on the right-hand side is associated with surface albedo and accounts for other diffuse scattering processes. The values of the C_i coefficients are tabulated in Table 3-1. Although the coefficients tabulated on Table 3-1 describe the mean model since they were based on mean radiances, the C_i coefficients will vary because of the variations that exist in the atmosphere and the underlying surface. The diffuse part of radiation varies, depending upon the sea state, particles in suspension, and atmospheric turbidity. The Rayleigh scattering term is affected by variability of water vapor in the air, which causes changes in the absorption of radiation. The sea state, which is influenced by wind conditions, determines the width of the dispersion of radiances about the forward scattering peak, thus influencing changes in the specular term [27]. Because the terms in the empirical formula are expressed as sum and/or product of u and u_0, this form satisfies the principle of reciprocity. The expression works best for $uu_0 > 0.1$; however, in order to normalize the expression, it will be used over the full ranges of u and u_0.

The albedo can be computed from Eq. (3.1) by integrating it over the upwelling hemisphere (weighted by u). The BDRF integrates to π by the normalization condition, giving

$$a_0(\zeta) = C_1 + C_2 u_0^{-C_3}\left(\frac{3-u_0^2}{2-C_3} + \frac{3u_0^2-1}{4-C_3}\right) + \frac{D}{u_0^2} \qquad (3.2)$$

Table 3-1. Model coefficients for clear and partly cloudy over ocean

Scene Type	C_1	C_2	C_3	C_4	C_5	D
Clear Ocean [1]	0.010	0.023	0.800	0.0056	1.060	0.011
Clear Ocean [2]	0.005	0.027	0.900	0.0080	1.100	0.016
PC over Ocean [3]	0.040	0.047	0.577	0.0080	1.157	0.016

[1] Applied analytic fit to ERBE operational models
[2] Tuned to alongtrack data (Dlhopolsky model)
[3] PC - Partly Cloudy

The last term, which is due to the forward reflection from the ocean surface, is an approximation to the integral, and is independent of C_4. This is because although the radiance is dispersed around the forward scatter peak by an amount depending on C_4, the total contribution to the reflected flux is the same. The computation of D is discussed in Appendix A.

Another factor that induces changes in the BDRF is cloud contamination of the scene. ERBE scene identification algorithms classify a scene as clear if the amount of cloud coverage varies between 0 and 5%. In order to account for cloud contamination in clear ocean scenes, the bidirectional reflectance is taken to be [26]

$$r(model) = C_6 r_C + (1 - C_6)\, r_0(\theta, \phi, \zeta) \tag{3.3}$$

where C_6 is the effective cloud amount within the field of view. The coefficient r_c is the reflectance for cloud, and $r_0(\theta,\phi,\zeta)$ is given in Eq. (3.1). C_6 varies from 0 to 5% for clear ocean. The cloud reflectance used is for middle altitude water (MW) clouds, computed by Staylor[13]. The correlation of the bidirectional reflectance with the scattering angle was shown on Figure 2-4 for variable cloud heights. The corresponding cloud albedo has been evaluated by Green and Smith [28] and is given by

$$a(\zeta) = 2Y_0 u_0^{-1} + 2Y_1 u_0^{n-1} I(u_0, N) \tag{3.4}$$

where $Y_0 = 0.005$, $Y_1 = 1.346$ and N=1.577 for MW clouds and

$$I(u_0, N) = \int_0^1 \left(\frac{u}{u + u_0} \right)^N du \tag{3.5}$$

The corresponding albedo for clear ocean is computed as [26]

$$a(model) = C_6 r_c + (1 - C_6)\, a_0(\zeta) \tag{3.6}$$

Because some of the NIMBUS 7 shortwave data was missing or considered questionable due to inadequate sampling, various methods to fill in these angular bins were implemented and flagged. Data restrictions were imposed in fitting the NIMBUS 7 tabulations for the development of the analytic model. The flagged bins were not utilized as well as bins in which $uu_0 < 0.1$. Solar zenith angle bins in which the scene type is questionable were also eliminated (e.g. $u_0 < 0.3$ might either be ice or snow and not ocean surface).

3-2. Analytic Form of BDRF for Land, Snow, Desert, Mostly Cloudy over Ocean and Overcast Scenes

The bidirectional reflectance for land, snow, desert, mostly cloudy over ocean, and overcast scenes is given by [26]

$$r(model) = \omega r_{Ray} + \Psi\left[\frac{\Delta r}{\Psi}(model)\right] \tag{3.7}$$

where r_{RAY} is the bidirectional reflectance due to Rayleigh scattering (second term in Eq. (3.1) and Ψ, the azimuthal mean reflectance, is given by

$$\Psi = \frac{1}{\pi}\int_0^{\pi} \Delta r d\phi \tag{3.8}$$

where $\Delta r = r_{ERBE} - r_{RAY}$. The ERBE operational bidirectional reflectance, r_{ERBE}, is computed from the tabulation of Suttles et al.[16]. For scenes with cloud cover, Rayleigh scattering is reduced due to the decreased amount of atmosphere above the reflecting surface. For a completely overcast scene (i.e. cloud amount > 95%), the mean cloud tops are at 680 mb, thus 2/3 of the Rayleigh model as determined over the ocean is used. As the cloud amount decreases, the amount of Rayleigh scattering increases. The weighting factor ω describes the reduction in Rayleigh

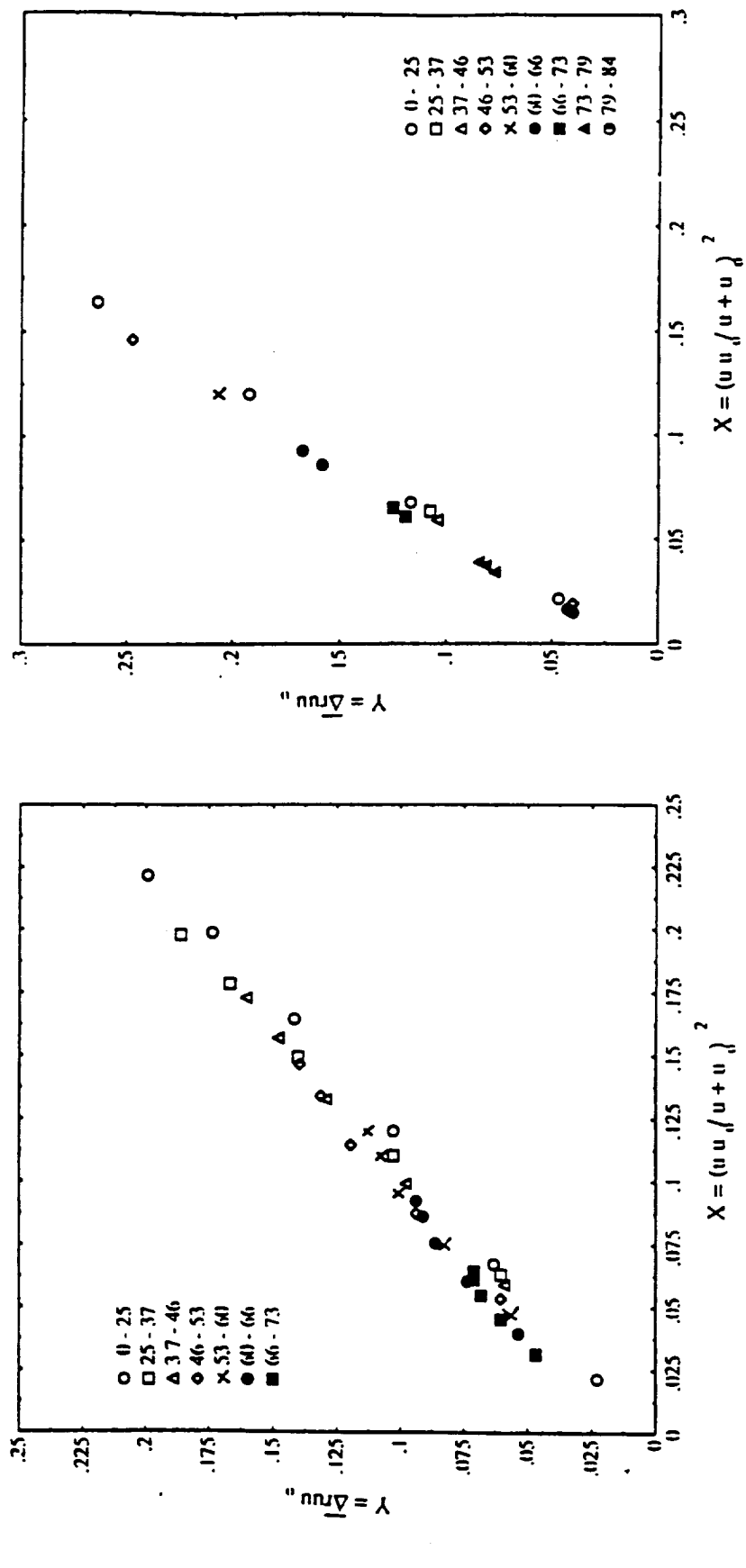

(a) Mostly Cloudy over Ocean

(b) Overcast

Figure 3-1. Correlation of directional reflectance with directional angles.

scattering effects due to increased cloudiness. The azimuthal mean reflectance Ψ can be expressed in terms of the viewing zenith and solar zenith angles by [13]

$$Y = A + Bx^2 \tag{3.9}$$

where $Y = \Psi u u_0$ and $x = \frac{u u_o}{u + u_o}$. Staylor [13] discusses the significance of the A and B regression coefficients. Figures 3-1(a,b) depict the correlation of the directional reflectance with the zenith angles for mostly cloudy over ocean and overcast scenes, respectively. The regression coefficients are very close to 1.0 for both cases. As in Staylor's desert and cloud bidirectional reflectance models, the combination of the sum and products of u and u_0 satisfy reciprocity. The last term of Eq. (3.1) is computed from the following expression [13]:

$$\frac{\Delta r}{\Psi}(model) = \frac{1 + K(G + \cos\gamma)^2}{1 + K\left[G^2 - 2Guu_o + (uu_o)^2 + \frac{1}{2}(vv_o)^2\right]} \tag{3.10}$$

where G determines where the model has its minimum value and K is the model amplitude.

As in the clear and partly cloudy over ocean cases, restrictions on the NIMBUS 7 data were imposed to exclude questionable scene types, angular bins that have no sampling or sparse population, and angular bins whose ADMs were calculated using any one of the interpolation techniques discussed above.

The model coefficients for these scene types, as well as the Rayleigh weighting factors, are tabulated on Table 3-2.

Similarly, the model albedo *a (model)* is computed using the relation [26]

$$a(model) = \omega a_{Ray} + \Delta a \tag{3.11}$$

where the albedo contribution of Rayleigh scattering is the second term in Eq. (3.2) and Δa is expressed as

$$\Delta a = 2\frac{A}{u_o} + 2Bu_o\left[1 + u_o - 2u_o ln\,(1 + u_0) + 2u_o lnu_o - \frac{u_o^2}{1 + u_o}\right] \qquad (3.12)$$

The BDRF is finally computed by dividing the bidirectional reflectance by the albedo.

The model albedos, computed from Eq. (3.11), are plotted in Fig. 3-2 as a function of solar zenith angle. All scenes exhibit an increase of model albedo with increasing solar zenith angle, although clear snow does not increase significantly as do the other scenes. Clear land is not a highly reflective surface due to the presence of vegetation. Clear desert is a brighter surface since it is generally composed of light sand and little or no vegetation. These model albedos are in good agreement with those determined for the ERBE operational directional models.

Table 3-2. Model coefficients for land, snow, desert, mostly cloudy over ocean, and overcast scenes

Scene Type	A	B	G	K	ω
Clear Land	0.002	0.384	0.138	0.650	1.000
Clear Snow	0.011	2.517	0.675	0.188	1.000
Clear Desert	-0.003	0.784	0.025	0.412	1.000
PC over Land*	0.009	0.643	0.350	0.875	0.917
MC over Ocean**	0.025	0.812	0.525	0.988	0.758
MC over Land	0.030	1.019	0.643	0.988	0.758
Overcast	0.024	1.530	0.550	0.625	0.668

* PC - Partly Cloudy
** MC - Mostly Cloudy

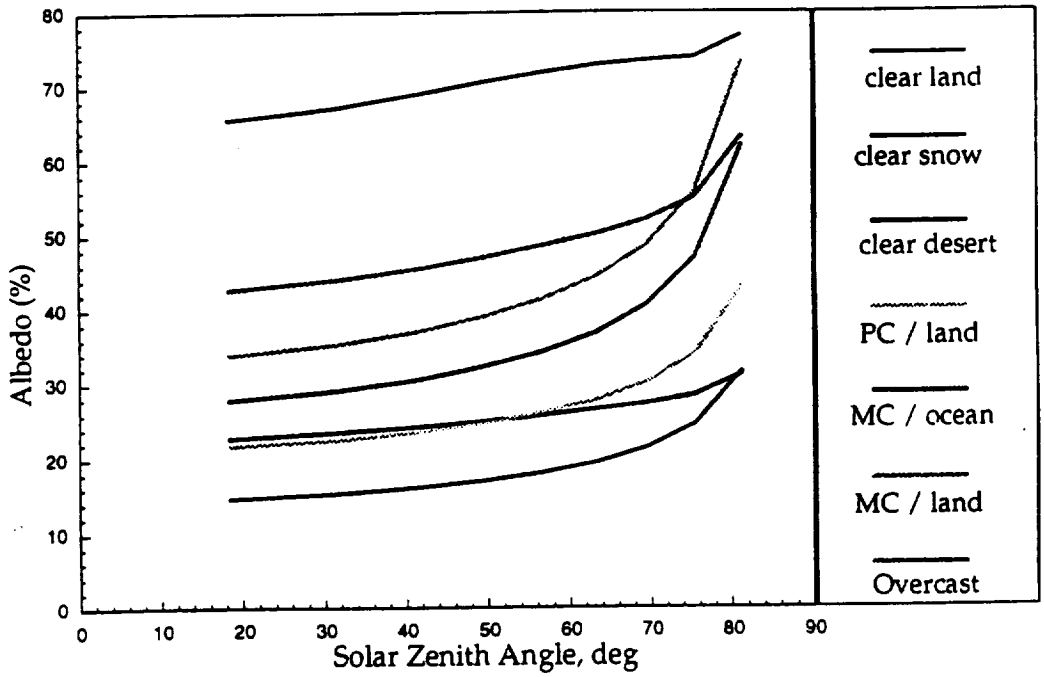

Figure 3-2. Model albedo for selected ERBE scene types.

Chapter 4
VALIDATION AND RESULTS

In order to validate the analytic BDRFs, these models are compared with the ERBE operational BDRFs. The effectiveness of these models in accounting for anisotropy at the limb when the same site is observed from a number of viewing directions is evaluated with alongtrack data. A brief description of this experiment is presented. Validation results for ocean under varying degrees of cloud cover and overcast scene are shown. The shortwave radiance standard deviations (SWR σ) are also computed.

4-1. Alongtrack Data

4-1.1. Alongtrack Scan Experiment

During limited periods in January and August 1985, the scanning radiometers on ERBE were rotated in azimuth so as to scan along the orbit track rather than crosstrack. Operation in the alongtrack mode allows for the collections of data applicable to radiation directionality studies. This mode, shown on Fig. 4-1, shows that a single site on the ground track can be viewed from a number of viewing zenith angles during an orbital pass. Alongtrack data are ideal for validating the ancillary data needed to analyze radiometric measurements. However, the orbit geometry constraints inhibit full angular coverages. The scan mode does not allow for the sun within 15° of the orbit plane (i.e. no data was collected for relative azimuths within 15° of the principal plane) where there is strong forward and backward scattering.

In order to apportion the radiance measurements, the orbit track is divided into 16-second intervals along the ground track. An interval is approximately 108 km. long and corresponds to a pixel length at a viewing zenith angle of 55°. A pixel is assigned to the interval in which its center falls, as depicted on Fig. 4-2, regardless

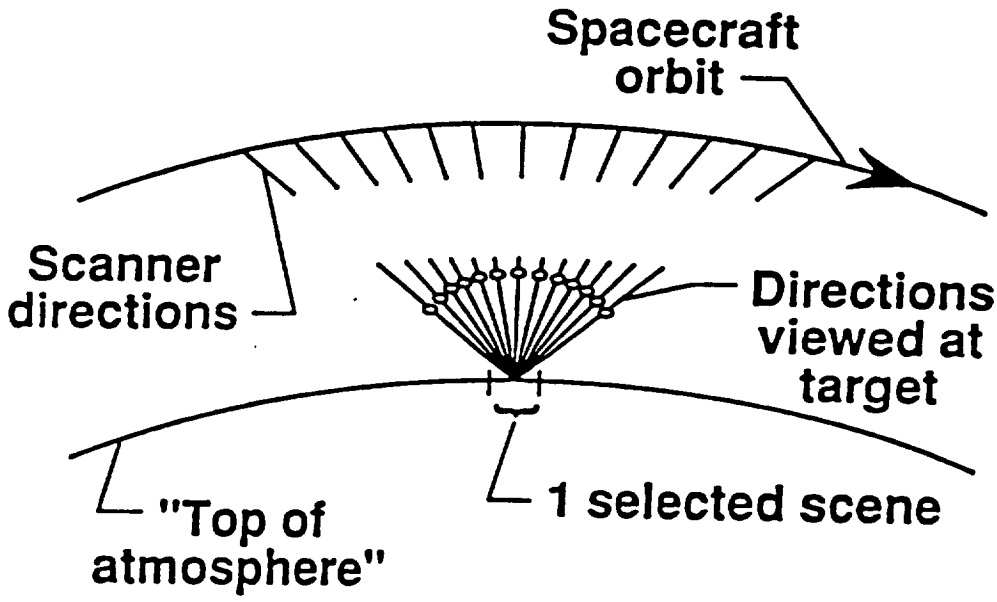

Figure 4-1. Use of alongtrack data for multiple views of a scene.

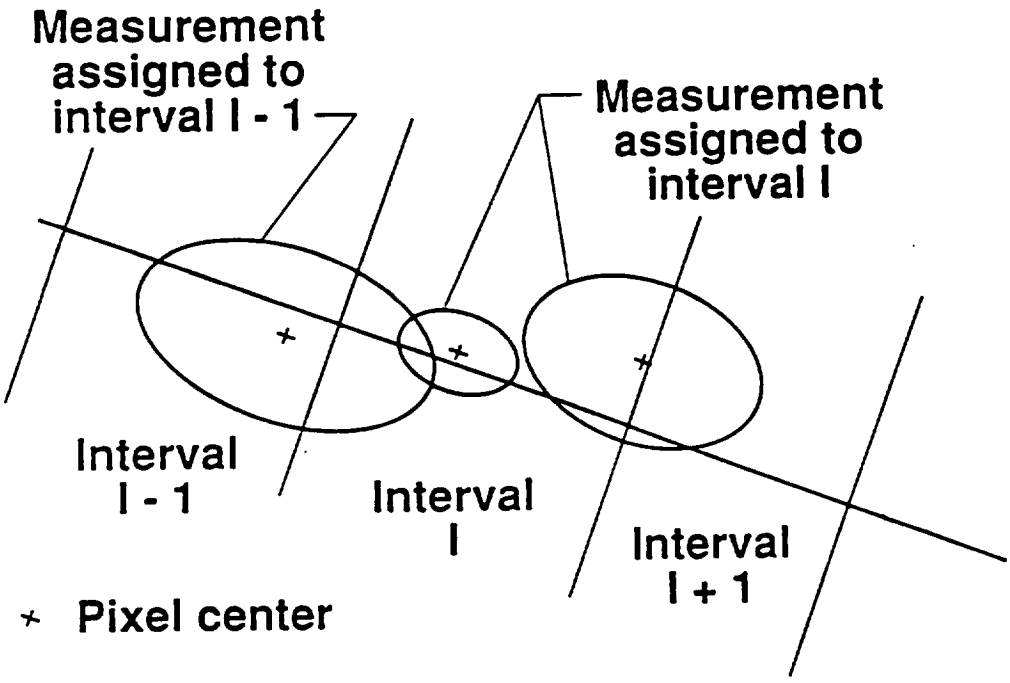

Figure 4-2. Allocation of measurements to alongtrack intervals.

of how much of the pixel falls in adjacent intervals. Each interval has approximately 250 pixels assigned to it.

The scene type of the pixels are computed by the ERBE scene identification algorithm [1]. The interval scene type is determined by compiling the pixels within 10° of the viewing zenith angle and if 80% of these pixels agree in scene, the scene type with the highest scene agreement is selected to be the interval scene. Intervals which do not meet this criterion are not used. This requirement assures that the interval has a uniform scene type across it.

In a three-dimensional broken cloud field, apparent cloudiness increases with increasing viewing zenith angles (Fig. 4-3). With the alongtrack data, the scene can be identified near nadir, which is an advantage of this dataset.

4-1.2. Validation of Fluxes with Alongtrack Data

Alongtrack scan data is useful in determining the effectiveness of BDRFs at different viewing zenith angles since a target area can be viewed from a number of viewing zenith angles. A target area, viewed from nadir and from off-nadir, gives two different radiance measurements but must be converted to the same flux by a correctly-modeled BDRF.

To validate the analytic BDRF, the ERBE alongtrack radiances are converted to TOA flux as a function of the viewing zenith angle. For a given alongtrack interval, the fluxes are normalized to near zenith fluxes to produce flux ratios. Since the same area is being viewed, only at different view angles, a flux ratio equal to 1.0 signifies correct modeling of the BDRFs.

4-1.3. Presentation of Results

The patterns of bidirectional reflectance functions and shortwave radiance standard deviations are presented on polar contour diagrams. The patterns are constructed for each scene type (clear, partly cloudy, mostly cloudy over ocean

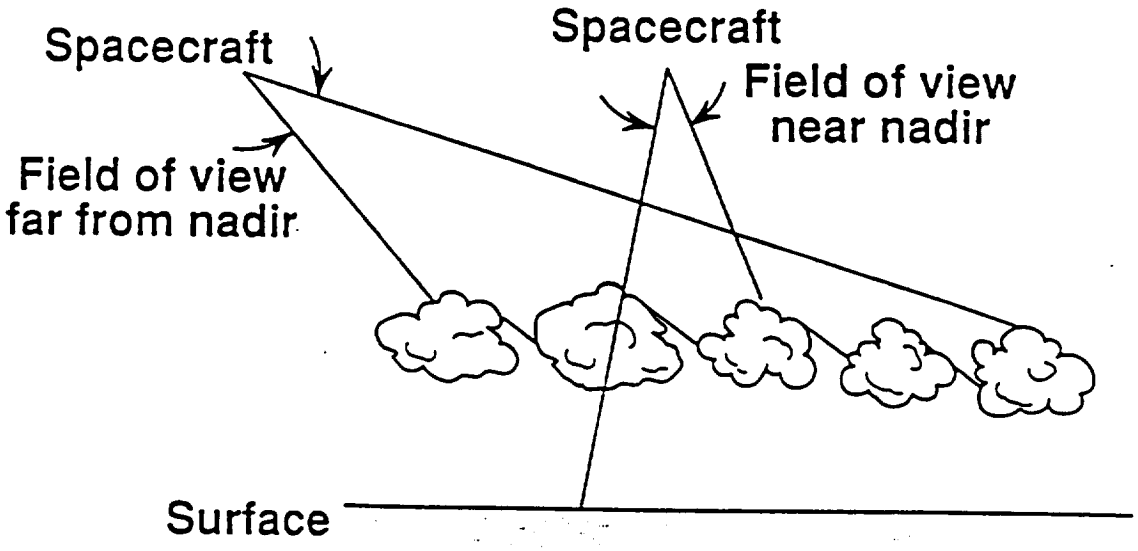

Figure 4-3. Effect of viewing zenith angle with apparent cloudiness.

and overcast) and solar zenith angle range defined by Suttles et al. [16]. The radial coordinates correspond to the satellite zenith angle θ while the angular coordinates represent the relative azimuth angle ϕ between the satellite and the sun. Figure 4-4 shows the coordinates and the angular bins of the ERBE operation models. The sun lies at ϕ=180° such that forward scattering corresponds to ϕ=0° while backward scattering is in the ϕ=180° region. Assuming that the reflection pattern is symmetric about the principal plane, only ϕ=0-180° is shown.

Although restrictions were imposed on the ERBE tabulated models to remove questionable data, the BDRF and SW radiance standard deviation were determined for all combinations of viewing and incident angles.

The analytical BDRFs represent the mean values within the angular bins for n=200 realizations. These models are computed for a set of random illumination and viewing angles uniformly distributed over the solar zenith, viewing zenith, and relative azimuth angle bins. Similarly, the ERBE models that are plotted correspond to the bin mean values determined by trilinearly interpolating over the given random illumination and viewing angles rather than the tabulated ERBE BDRFs. Instrument noise, in the order of 1-2 $Wm^{-2}sr^{-1}$, were taken into account in the radiance calculations.

For the BDRF plots, presented in the next section, the color bar below each set of contour plots indicate the BDRF range (0.5 - 2.0). The left portion of a contour polar diagram represents the analytical BDRF while the right portion represents the ERBE or Dlhopolsky mean BDRF. The angular bin BDRFs for each realization is converted into radiance from which the radiance standard deviations are computed. Meanwhile, SWR σ plots show two color bars; the left color bar gives the difference (Analytic - ERBE/or Dlhopolsky (clear ocean only)) in SWR σ while the color bar on the right gives the range of the absolute SWR σ. The left and right portions of the SWR σ contour plots correspond to the respective color bars described above.

Results of the validation with alongtrack data are presented as line plots of the flux ratios versus the viewing zenith angle for various solar zenith angle bin ranges. Flux ratios computed from the analytic and ERBE models are presented.

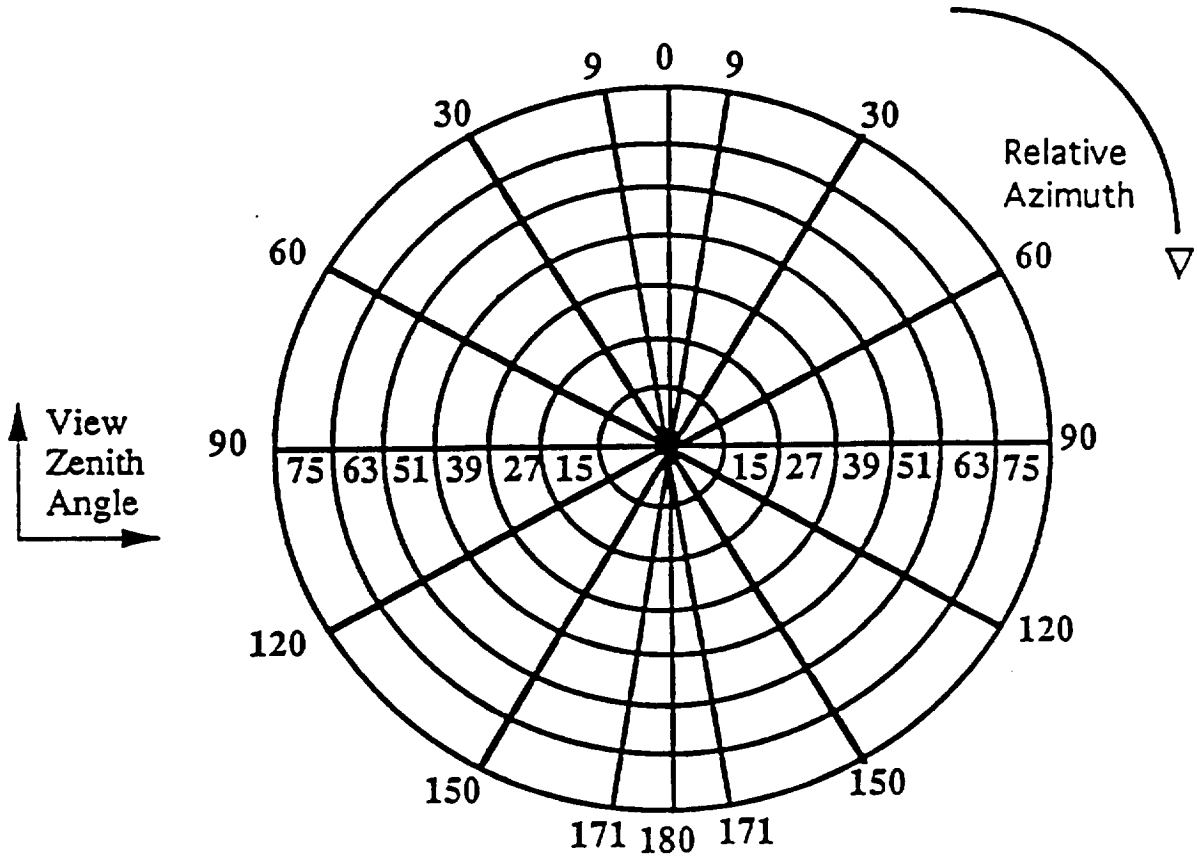

Figure 4-4. Coordinate system used in polar contour diagrams.

4-2. Clear Ocean

4-2.1. Clear Ocean (Untuned Analytic Model)

The model coefficients are C_1 = 0.010, C_2 = 0.023, C_3 = 0.800, C_4 = 0.0056 and C_5 = 1.06 (Table 3-1). In order to account for the variabilities about the mean of the coefficients brought upon by influences of the atmosphere and surface, statistical properties for the coefficients are defined. The diffuse part C_1 is assumed to be uniformly distributed between 0.005 and 0.015. C_2 and C_4 are constant. C_3 and C_5 were tuned to get standard deviations that will give a reasonable match to the ERBE operational BDRF. C_3 has a truncated normal distribution with a mean of 0.8 and a nominal σ of 0.075. Values of C_3 that exceed 0.9 or are less than 0.7 are excluded. C_5 has a truncated normal distribution with a mean of 1.06 and a nominal σ of 0.020. Values of C_5 that are less than 1.01 or are greater that 1.11 are rejected. Figures 4-5 (a-f) depict the mean BDRF for clear ocean for six solar zenith angle bins for model coefficients derived from a fit to Suttles [16] tabulation. For solar zenith angle range 0 - 26° and $\phi = 0°$, the largest BDRF occurs at $\theta = 25°$ for ERBE while the analytical BDRF is a maximum in the area of $\theta = 10°$. At small viewing zenith angles ($\theta < 30°$), BDRF decreases as the ζ increases. For large θ, however, BDRF increases significantly with increasing solar zenith angles. All ζ ranges exhibit an increase in anisotropy towards the limb (limb-brightening) except in the near zenith of the sun (specular region). This is attributed to atmospheric scatter towards the limb over a dark ocean surface. Forward scattering is more prominent than backward scattering. The surface is most nearly isotropic at ϕ=90°. Since the BDRF values are normalized, as limb-brightening becomes more apparent, other viewing angles exhibit a decrease in anisotropy to compensate for the brightening. The sunglint area shifts towards the limb as solar zenith angle increases. The analytic and ERBE BDRFs are in good agreement. The bias is in the order of -0.048 and the RMS is equal to 0.118.

Figures 4.6 (a-f) depicts the SWR σ computed from the analytic model. Both ERBE and the analytic models do not show a trend in σ from one SZA bin to

another. However, as anisotropy increases, so does the σ. The largest difference occurs in the forward scatter direction towards the limb for $\zeta > 37^{\circ}$. For $\zeta < 37^{\circ}$, the differences in the specular region is in the order of 4-10 $Wm^{-2}sr^{-1}$. Generally, for the backscatter region and $\phi > 35^{\circ}$, the difference is in the order of + 2 $Wm^{-2}sr^{-1}$.

The effects of wind speed are depicted on Figs. 4-7 (a-b) for two solar zenith angle bins. The variability of wind affects how the forward scatter peak behaves. The amount of wind is imposed on the model by varying the value of C_5 in Eq. (3.1). For low wind speed, C_5 is set to 1.06 while for high wind speed, C_5 is set to 1.15. For very low wind, the sea surface is almost mirror-like, giving a sharp reflectance peak. For high winds, the sea surface is rough, thus making the forward scatter peak broader. Aside from differences in the behavior of the specular region, the wind does not appear to influence the BDRF pattern towards the limb in the backscatter direction nor near zenith.

A comparison of the alongtrack flux ratios (Figs. 4.8 (a-h)) for ERBE, Dlhopolsky, and the analytic models, show that the Dlhopolsky model produces flux ratios that are more nearly constant towards the limb than either of the other two models. This is especially true in the backward scatter direction. The ERBE models account for anisotropy in the forward scatter direction at $\zeta > 53^{\circ}$. The analytic model flux ratios show significant growth towards the limb. For $\zeta < 45^{\circ}$, the error at $\theta = 50^{\circ}$ is in the order of 15% and increases to 40% at $\theta = 70^{\circ}$. The error increases as the ζ increases.

4-2.2. Dlhopolsky vs. ERBE Clear Ocean Model

Figures 4.9 (a-f) illustrate the BDRF comparison between Dlhopolsky and ERBE for more refined solar zenith angle bins ($\Delta\zeta = 5^{\circ}$). Angular bins that were not sampled or deemed questionable by Dlhopolsky were not included in the plots, as shown by the black regions. The missing data includes angular bins that contain specular points, which were rejected by the Maximum Likelihood Estimate technique of scene identification procedure. For SZA < 25°, the ERBE models are grouped into a single solar zenith angle bin. The ERBE model does not account

accurately for the specular peak in this range. The peak occurs at $\theta = 25^\circ$ for ERBE in $0^\circ < \zeta < 5^\circ$ while Dlhopolsky's model shows a shift of the specular peak with increasing ζ as expected. For this range, the ERBE model will then overestimate the radiative fluxes. For $\zeta > 25^\circ$, both models compare well although the ERBE BDRF in the forward scatter region has a larger magnitude. A calculation of the differences between the two models showed that the largest biases occurred for $\zeta > 60^\circ$. The ERBE model is significantly less anisotropic in these solar angles than the Dhlopolsky model.

4-2.3. Clear Ocean (Tuned)

Using a least squares error method, the analytic model coefficients were tuned with alongtrack data using fluxes that were converted from observed radiances using the Dlhopolsky BDRF. The new coefficients are: $C_1 = 0.005$, $C_2 = 0.027$, $C_3 = 0.900$, $C_4 = 0.008$ and $C_5 = 1.10$. The corresponding statistical properties are as follows: a nominal $\sigma = 0.045$ and 0.002 for C_3 and C_5, respectively. Note that because the specular term coefficient C_4 increases from 0.0056 to 0.008, the approximation to the integral in the albedo specular term also is changed from $D = 0.011$ to $D = 0.0159$.

Figures 4-10 (a-f) compare the BDRF mean for the analytic model and Dlhopolsky model for the angular bins for which Dlhopolsky had adequate sampling. Angular bins of $5^\circ \times 5^\circ \times 5^\circ$ are used for presentation. Unlike the ERBE model for $\zeta < 25^\circ$, the region of specular reflection for the analytic model shifts accordingly with sun angle as Dlhopolsky model does. The Dlhopolsky model is more anisotropic in this region. Both exhibit limb-brightening at higher solar angles although the analytic model is more anisotropic in this region. At near zenith, both models are in good agreement. The bias and RMS are 0.005 and 0.110, respectively.

The flux ratios (Figs. 4-11(a-h)) show that the tuned BDRF better accounts for anisotropy at the limb especially for $\zeta < 46^\circ$ and $\zeta > 60^\circ$.

4-3. Overcast

The mean model coefficients for overcast scenes are shown on Table 3-2. The model coefficients are A = 0.024, B = 1.530, G= 0.550, and K = 0.625. The Rayleigh weighting factor is 2/3 of the clear ocean Rayleigh model, assuming that the mean cloud tops are at 680 mb. For this study, there was no attempt to discriminate the overcast models by cloud optical thickness, cloud height, or cloud liquid water content.

The correlation of the scattering angle with the analytic BDRF is depicted in Fig. 4-12. Although the clouds are not classified by liquid water content as Staylor's categories [13], a comparison with his results shows that the overcast model falls into the low water (LW) category. The scatter diagram shows a strong forward scatter peak, minimum BDRF at $90^\circ < \gamma < 120^\circ$, and a leveling off to a BDRF value of 1.0 at the scattering angles greater than 120°. These results agree with Staylor's reflectance correlations.

The mean BDRFs are illustrated on Figs. 4-13 (a-f) for $\zeta < 66^\circ$. For $\zeta < 37^\circ$, clouds are limb-darkened in the backscatter direction while for $37^\circ < \zeta < 46^\circ$, clouds are almost isotropic with $\theta < 60^\circ$. In higher solar zenith angles, clouds become more anisotropic and limb-brightening features, especially in the forward scatter region, become more discernible. The bias is in the order of -0.03 and the RMS is 0.054.

The SWR σ are shown on the right portion of the contour plots on Figs. 4-14 (a-f). The σ decrease with increasing solar zenith angles. Additionally, as tthe instrument scans towards the horizon, σ decreases. The left half of the contour plots show the differences in SWR σ between the ERBE and analytic models. For $\zeta < 26^\circ$, the largest differences occur at the limb while for large incident angles, differences in the order of 25% are observed in the specular region.

The flux ratios shown on Figs. 4-15 (a-h) show that the BDRF generally effectively accounts for anisotropy to the limb. An improvement is observed for $\zeta < 37^\circ$ (Figs. 4-15 a,b).

4-4. Partly Cloudy over Ocean

The model coefficients, as tabulated on Table 3-2, are $C_1 = 0.040$, $C_2 = 0.0471$, $C_3 = 0.577$, $C_4 = 0.008$ and $C_5 = 1.157$. Figures 4-16 (a-f) compare the analytic and ERBE BDRFs. The peak of specular reflection is evident even in high sun angles. This specular peak shifts towards the horizon as the solar zenith angles increase. At this higher sun angles, weaker limb-brightening in the backscatter direction emerges. Limb-brightening in the forward scatter direction is very prominent and broad. Reflectance is nearly isotropic at the large viewing angles for $\phi = 90^\circ$ and becomes even less anisotropic near nadir. The bias is equal to 0.005 and the RMS = 0.110.

The flux ratios illustrated on Figs. 4-17 (a-h) show that the tuned BDRF matches the ERBE and shows an improvement at $\zeta > 60^\circ$ in the forward scatter direction.

4-5. Mostly Cloudy over Ocean

For mostly cloudy over ocean, the mean model coefficients are $A = 0.025$, $B = 0.812$, $G = 0.525$, and $K = 0.988$. A comparison of the ERBE and analytic BDRF is shown on Figs. 4-18 (a-f). For $\zeta < 37^\circ$, both models are nearly isotropic at $\theta < 60^\circ$. For $\zeta > 37^\circ$, limb-brightening is more prominent for the analytic than the ERBE functions. Both models exhibit limb-brightening for $\zeta > 53^\circ$ and the forward scattering peak is more pronounced. Near nadir, less anisotropy is observed.

The flux ratios (Figs. 4-19 (a-h)) show that the analytic BDRF is more effective than the ERBE models in accounting for anisotropy for $\zeta < 53^\circ$. Flux ratios using the ERBE operational models do not show significant albedo growth in the backscatter region as do the analytic models for $\zeta > 53$.

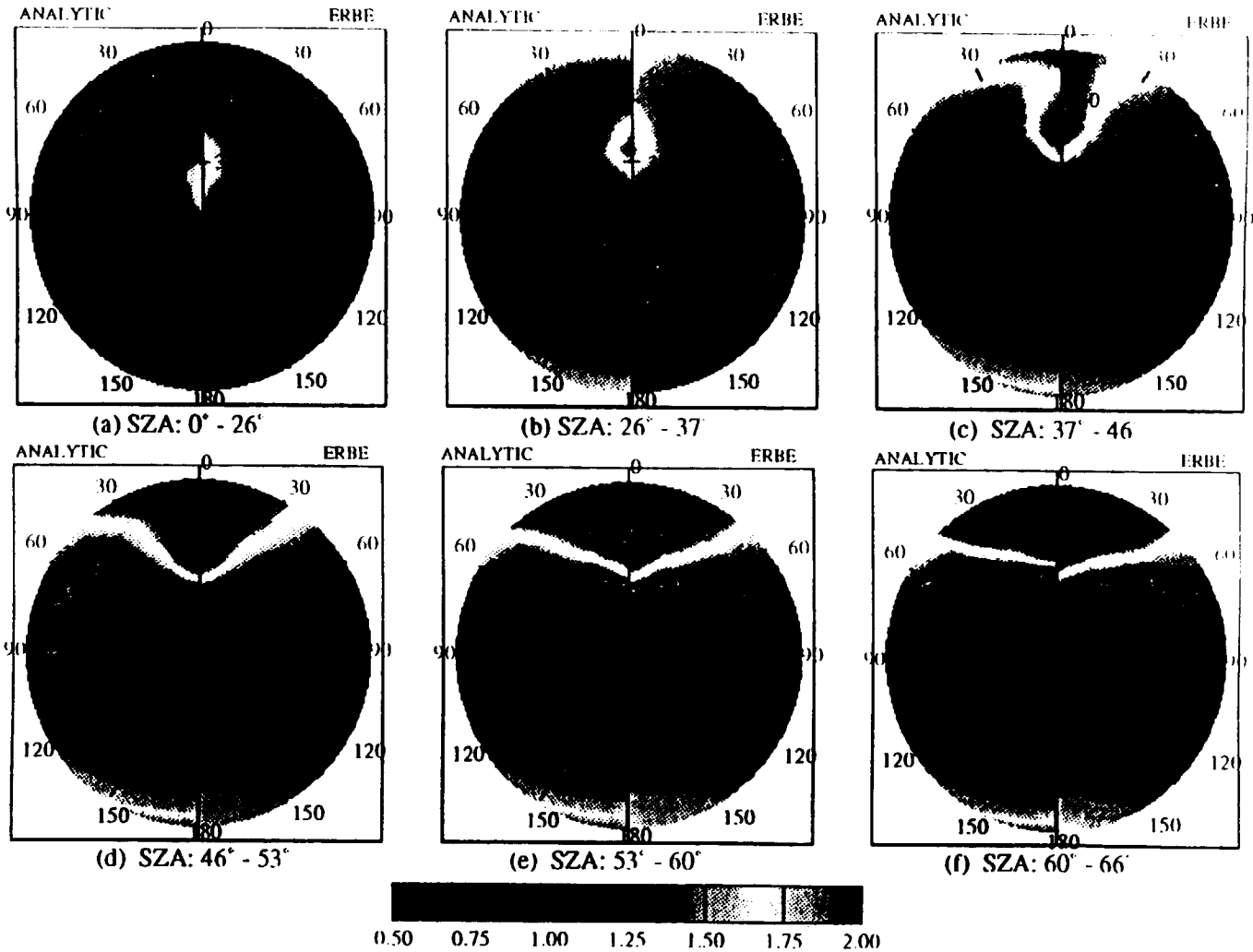

Figure 4-5. Comparison of analytic and ERBE BDRFs using nominal model coefficients for clear ocean ($C_1 = 0.01$, $C_2 = 0.023$, $C_3 = 0.800$, $C_4 = 0.0056$, $C_5 = 1.060$).

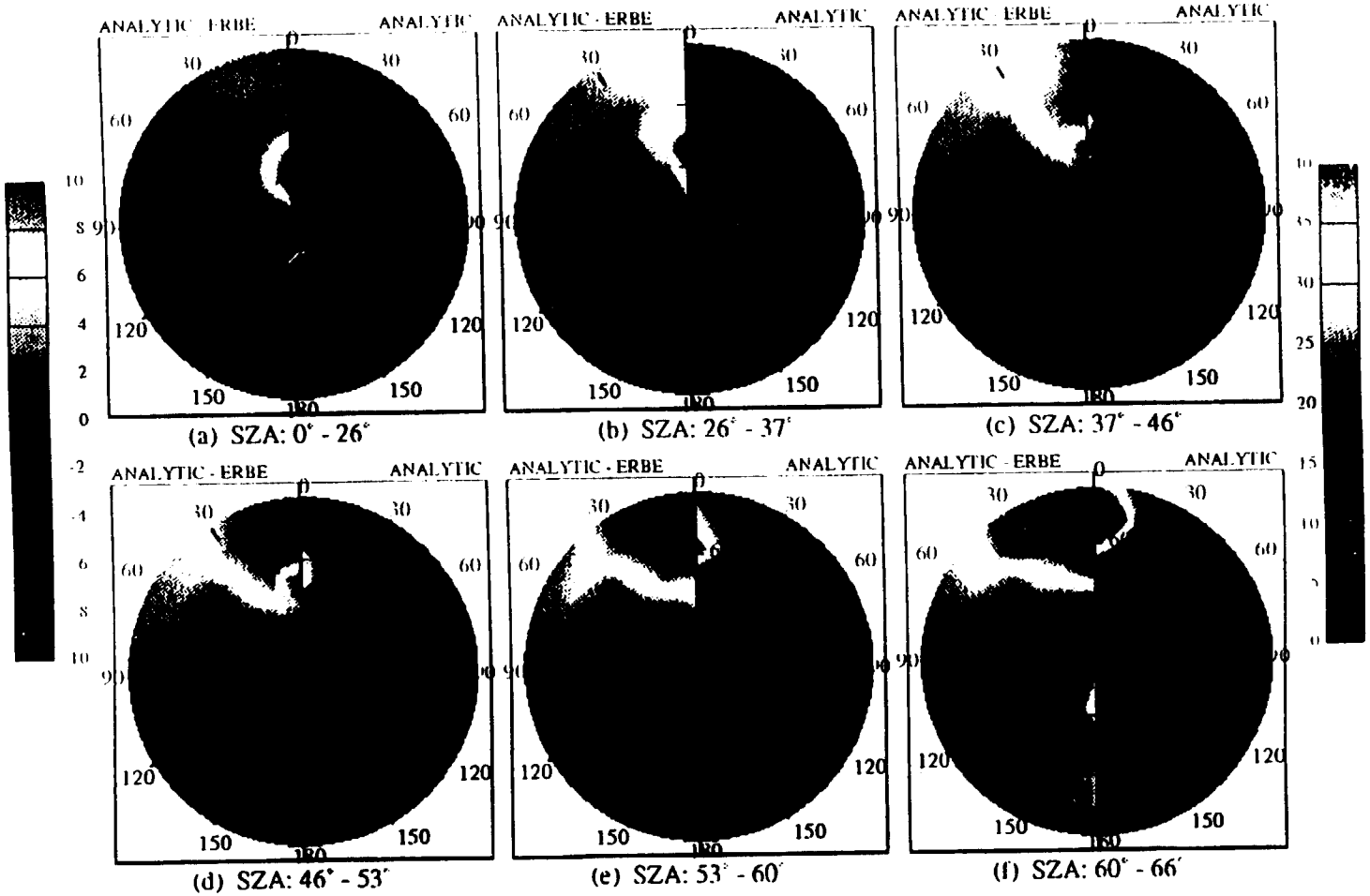

Figure 4-6. Comparison of shortwave radiance standard deviations from analytic and ERBE BDRFs for clear ocean ($C_1 = 0.01$, $C_2 = 0.023$, $C_3 = 0.800$, $C_4 = 0.0056$, $C_5 = 1.060$).

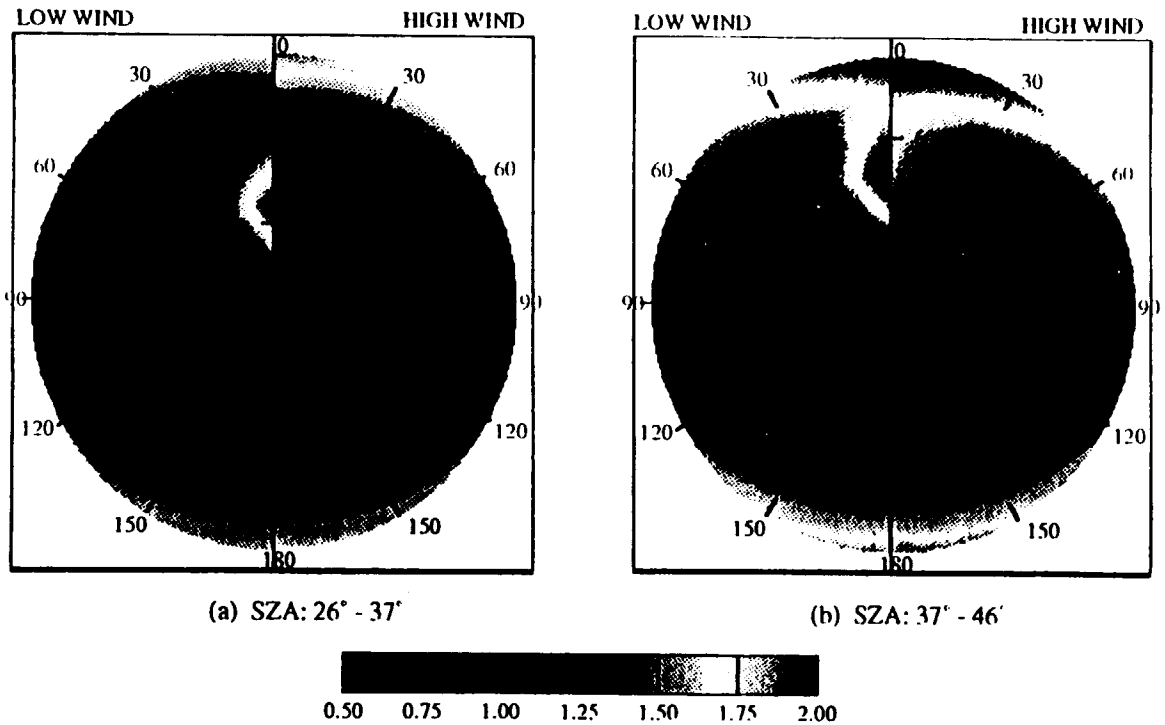

Figure 4-7. Wind speed effects on clear ocean BDRF .

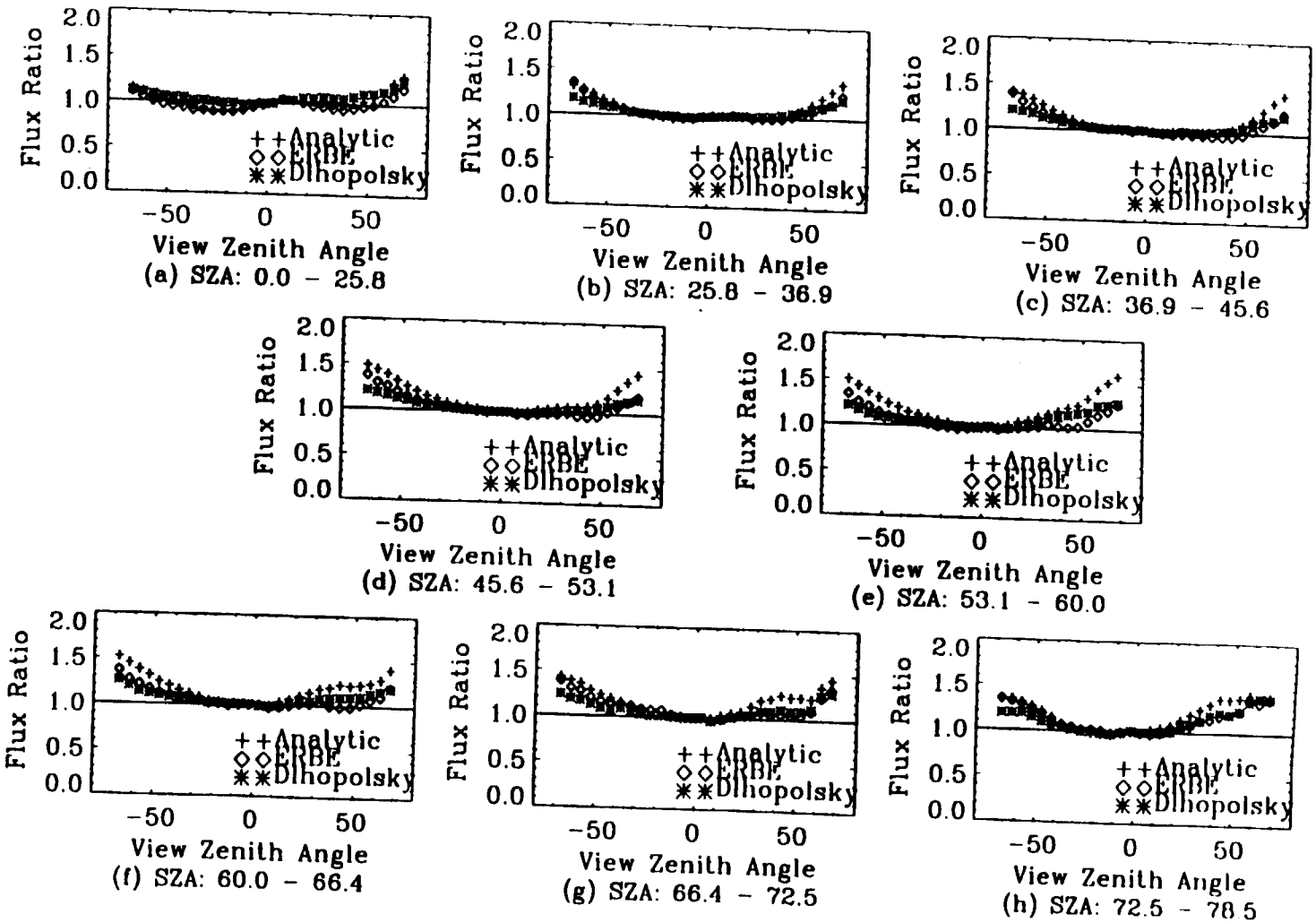

Figure 4-8. Ratio of alongtrack SW flux using the nominal model coefficients, ERBE BDRF and Dlhopolsky BDRF for clear ocean.

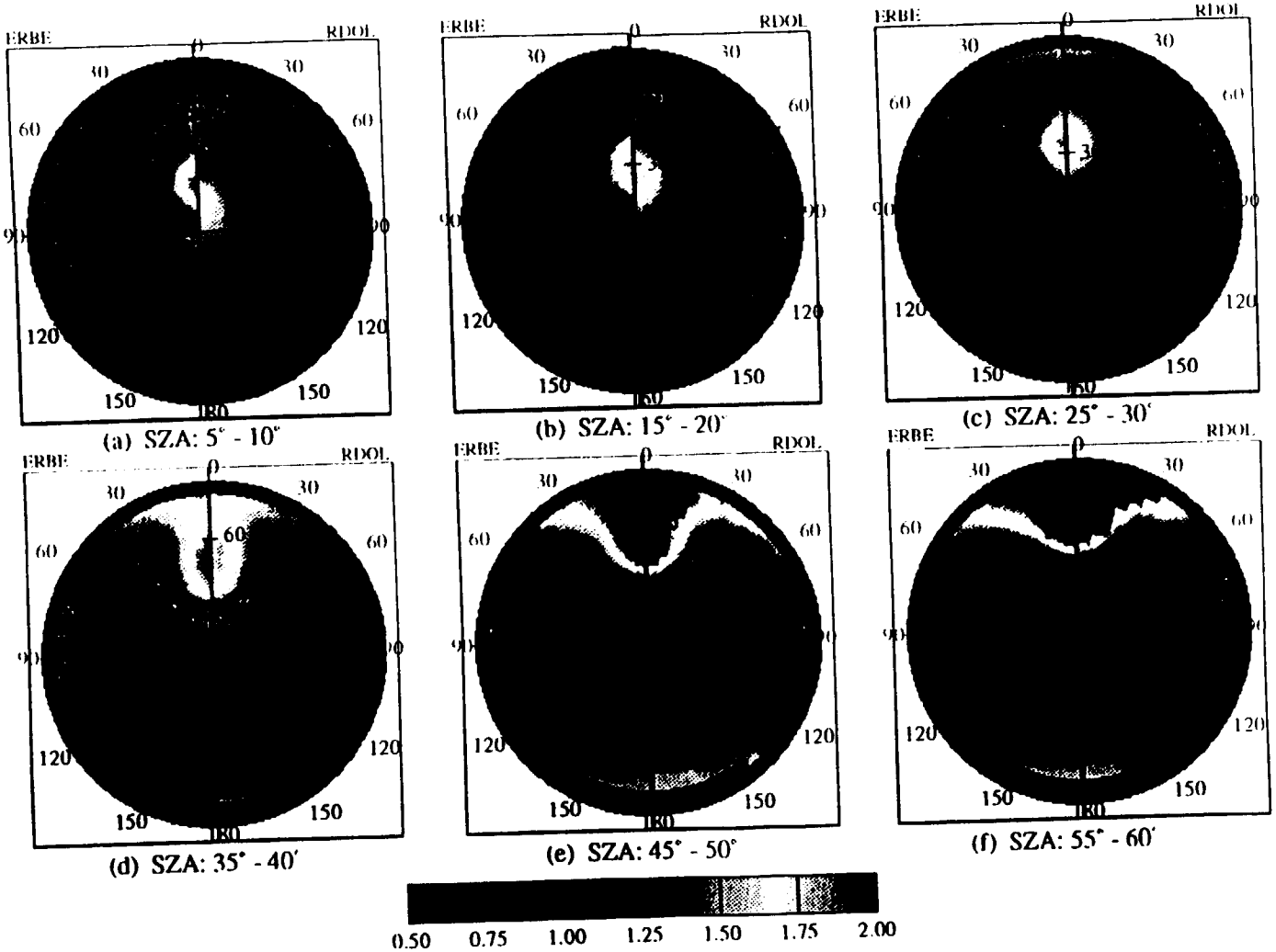

Figure 4-9. Comparison of ERBE and Dlhopolsky BDRF for clear ocean.

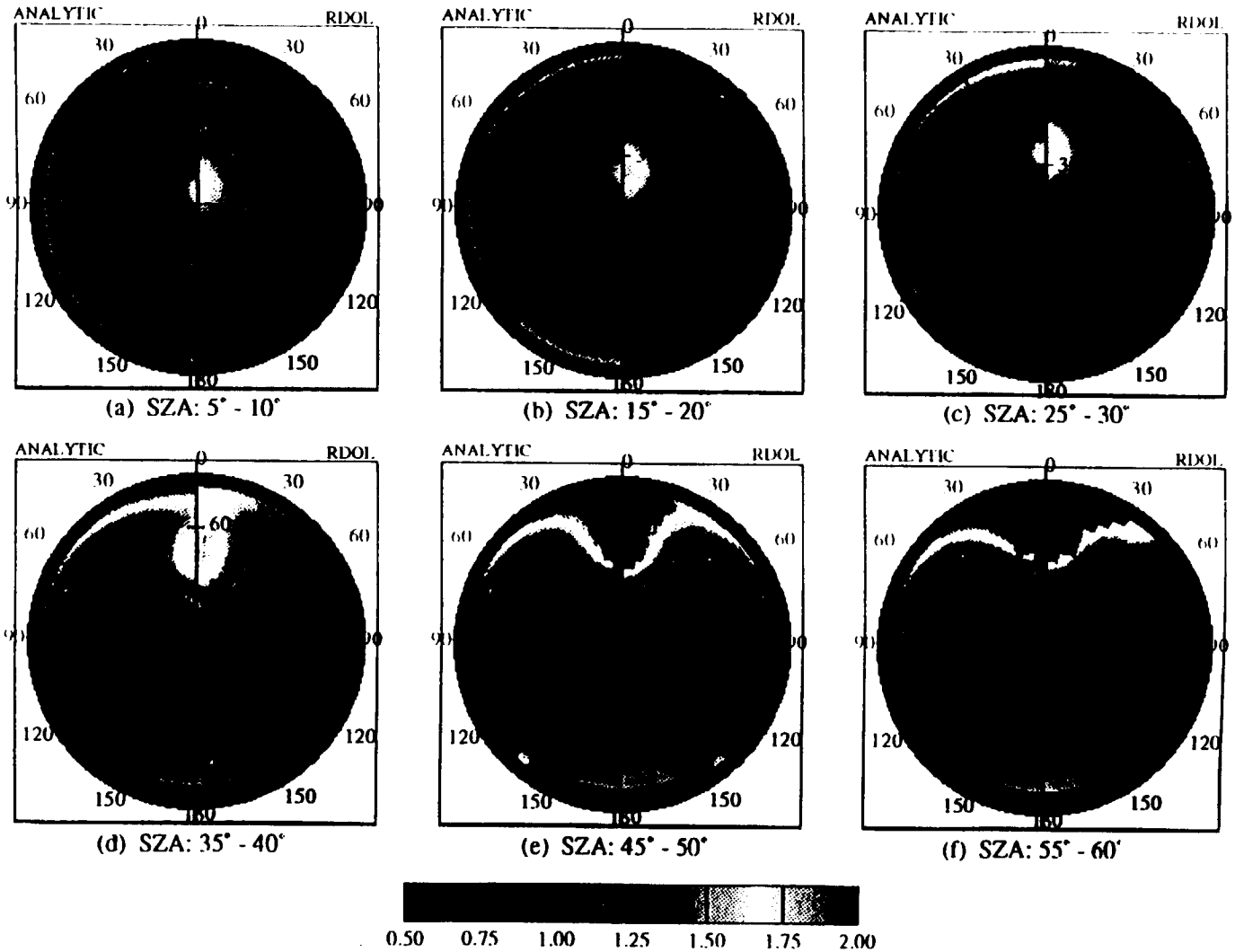

Figure 4-10. Comparison of analytic and Dlhopolsky BDRF for clear ocean ($C_1 = 0.005$, $C_2 = 0.027$, $C_3 = 0.900$, $C_4 = 0.008$, $C_5 = 1.100$).

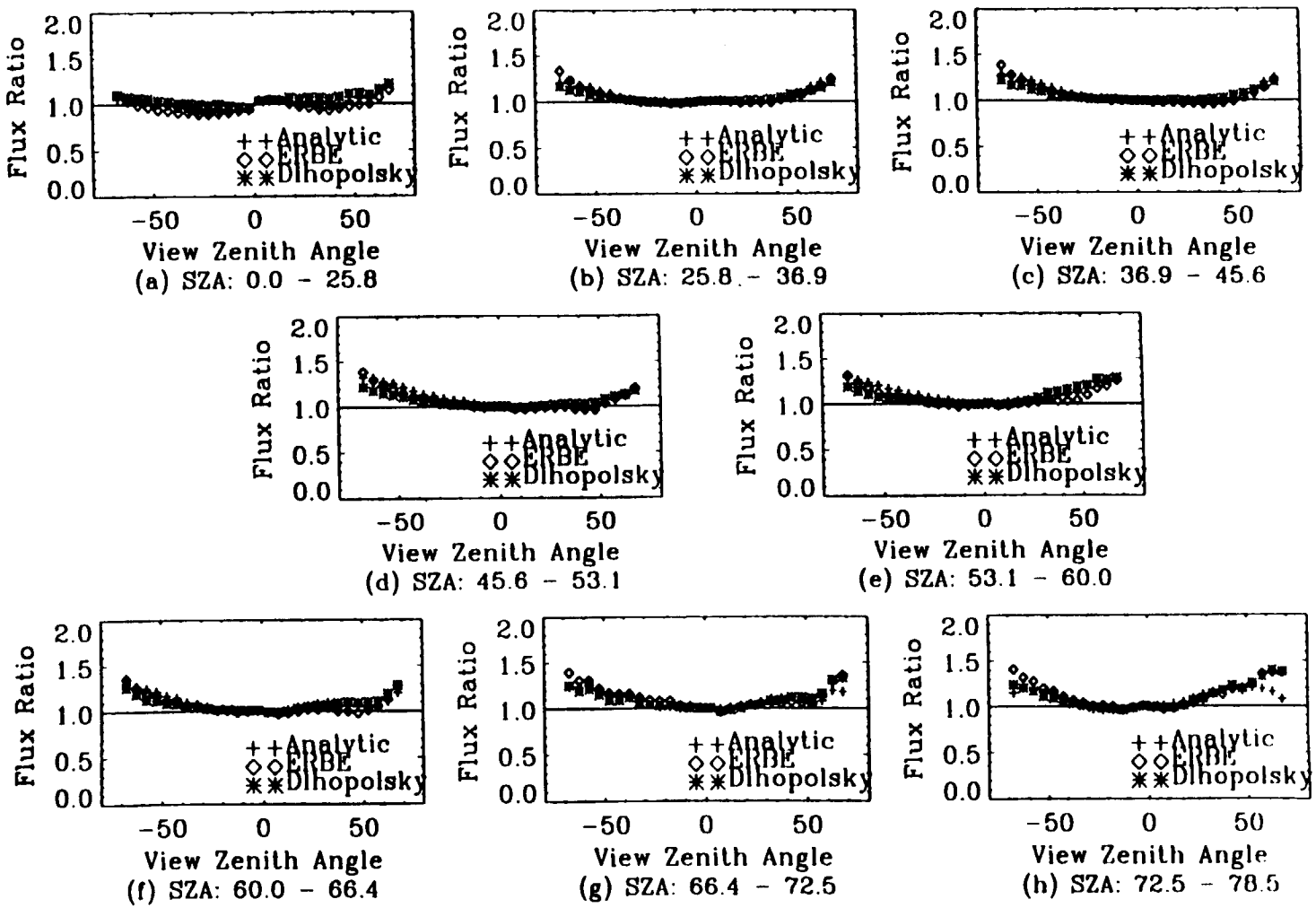

Figure 4-11. Ratio of alongtrack SW flux using the alongtrack-tuned model coefficients, ERBE BDRF and Dlhopolsky BDRF for clear ocean.

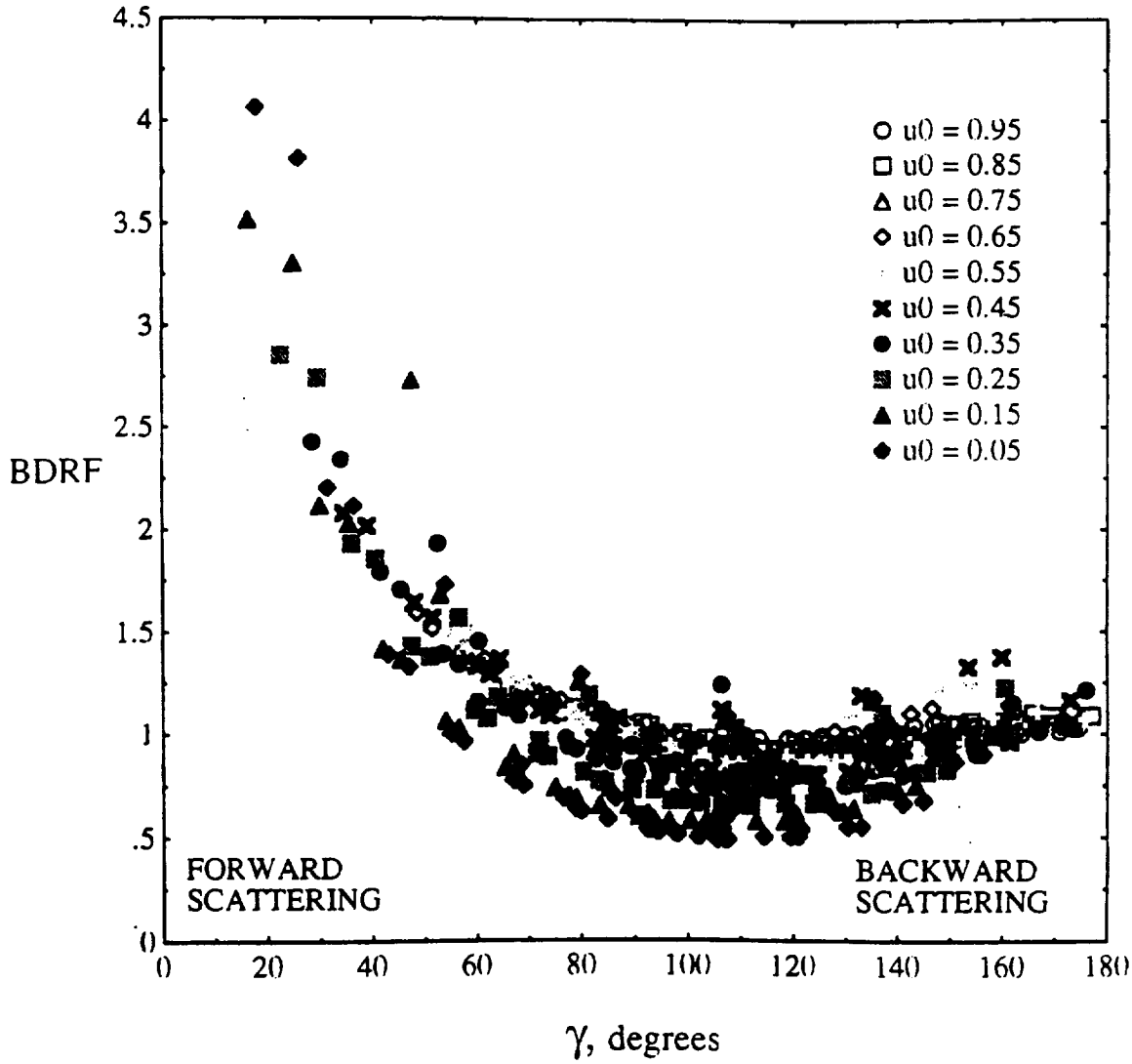

Figure 4-12. Correlation of analytic BDRF for overcast scene and scattering angle.

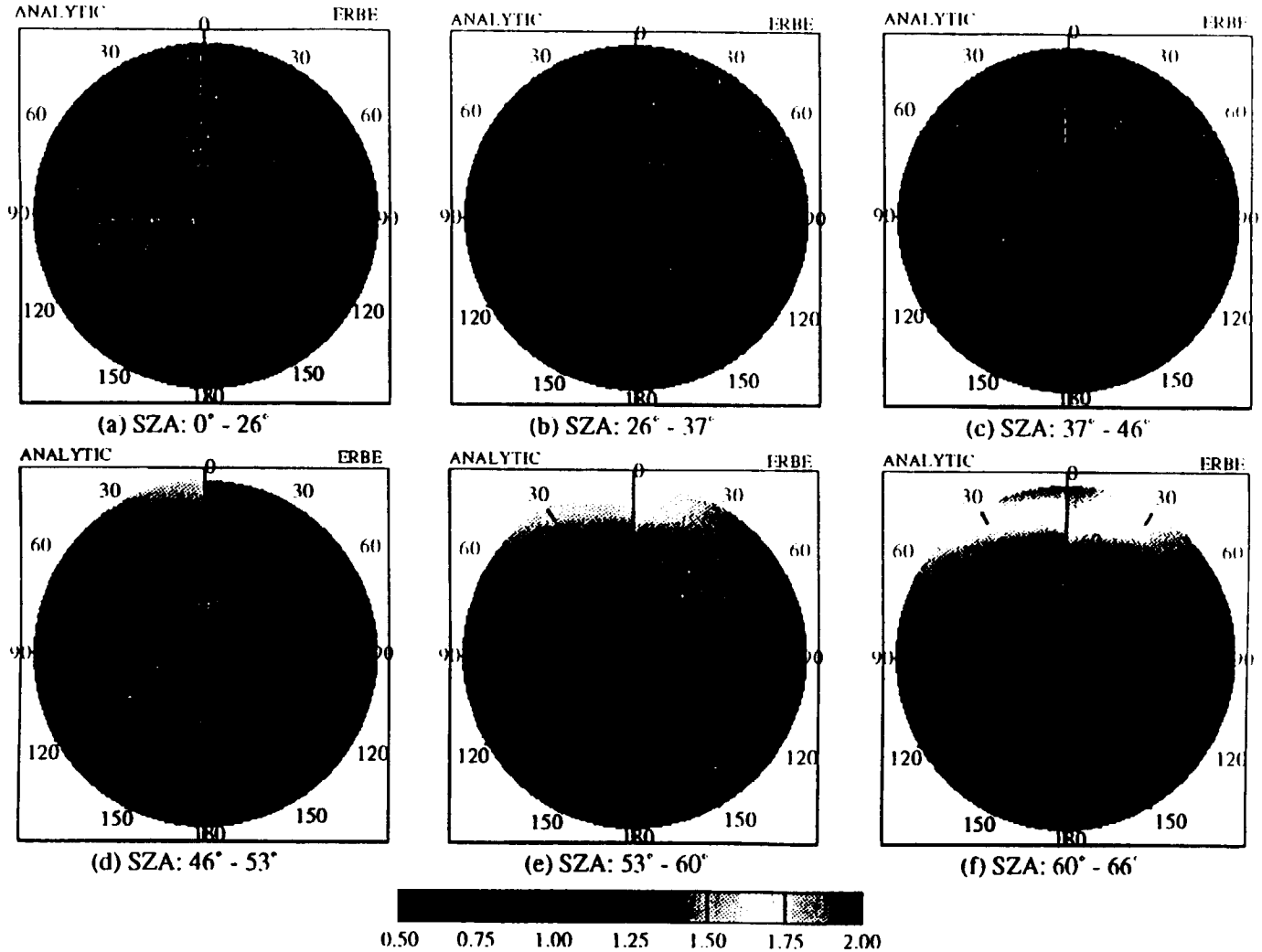

Figure 4-13. Comparison of analytic and ERBE BDRF for overcast scene (A = 0.024, B = 1.530, G = 0.500, K = 0.625, ω = 0.667).

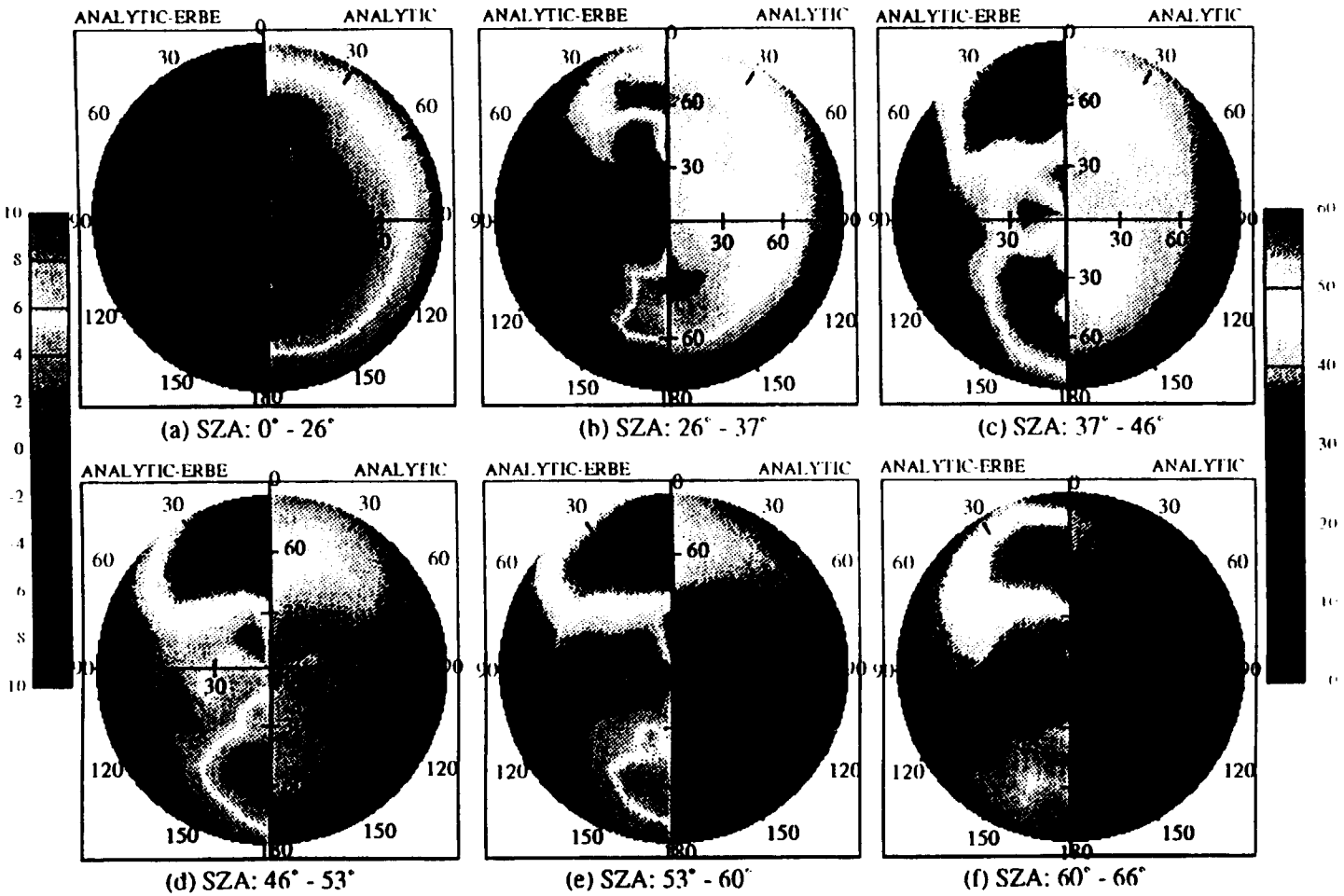

Figure 4-14 Comparison of shortwave radiance standard deviations from analytic and ERBE BDRFs for overcast scene (A = 0.024, B = 1.530, G = 0.550, K=0.625).

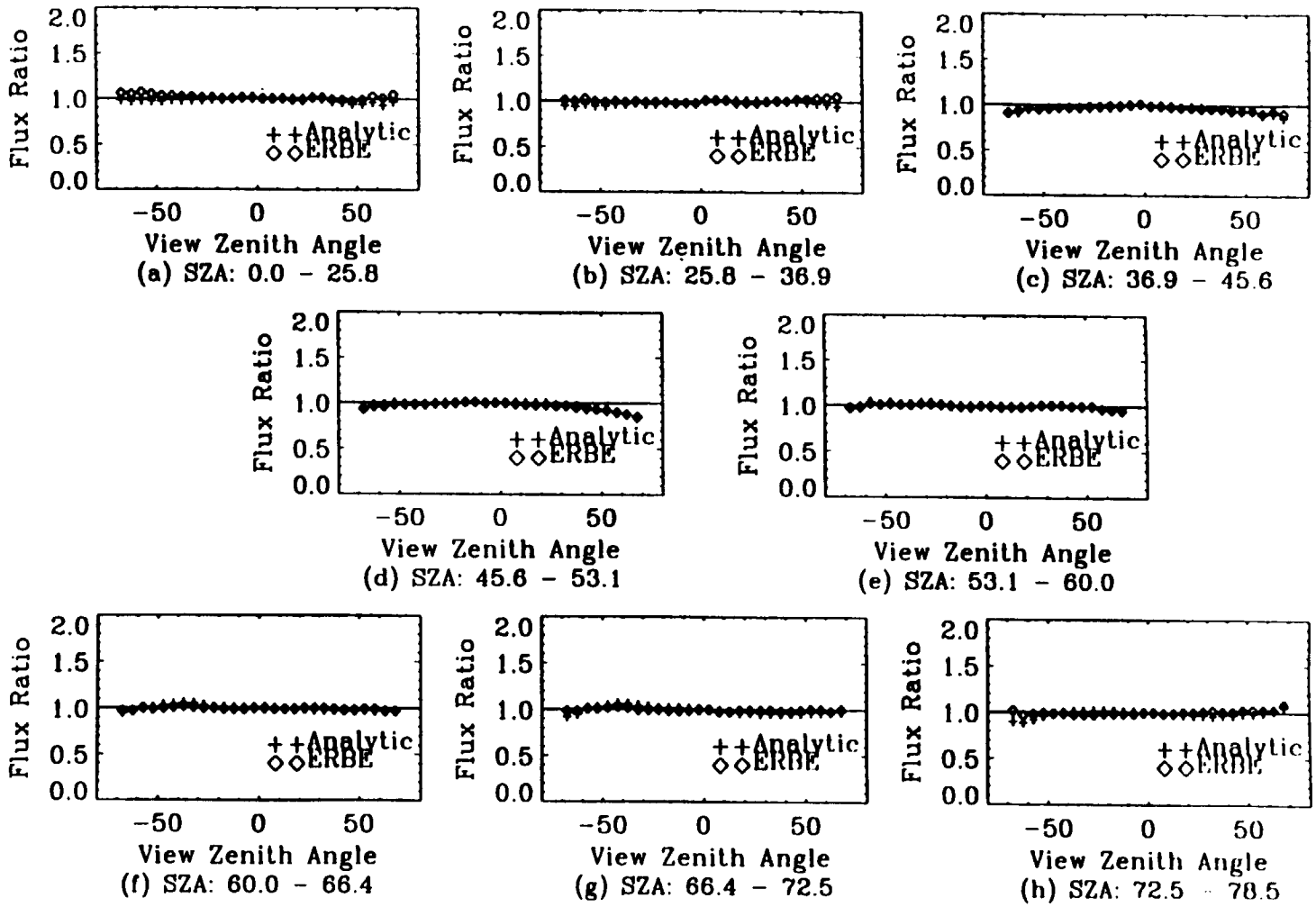

Figure 4-15. Ratio of alongtrack SW flux using the analytic and ERBE BDRF for overcast scene.

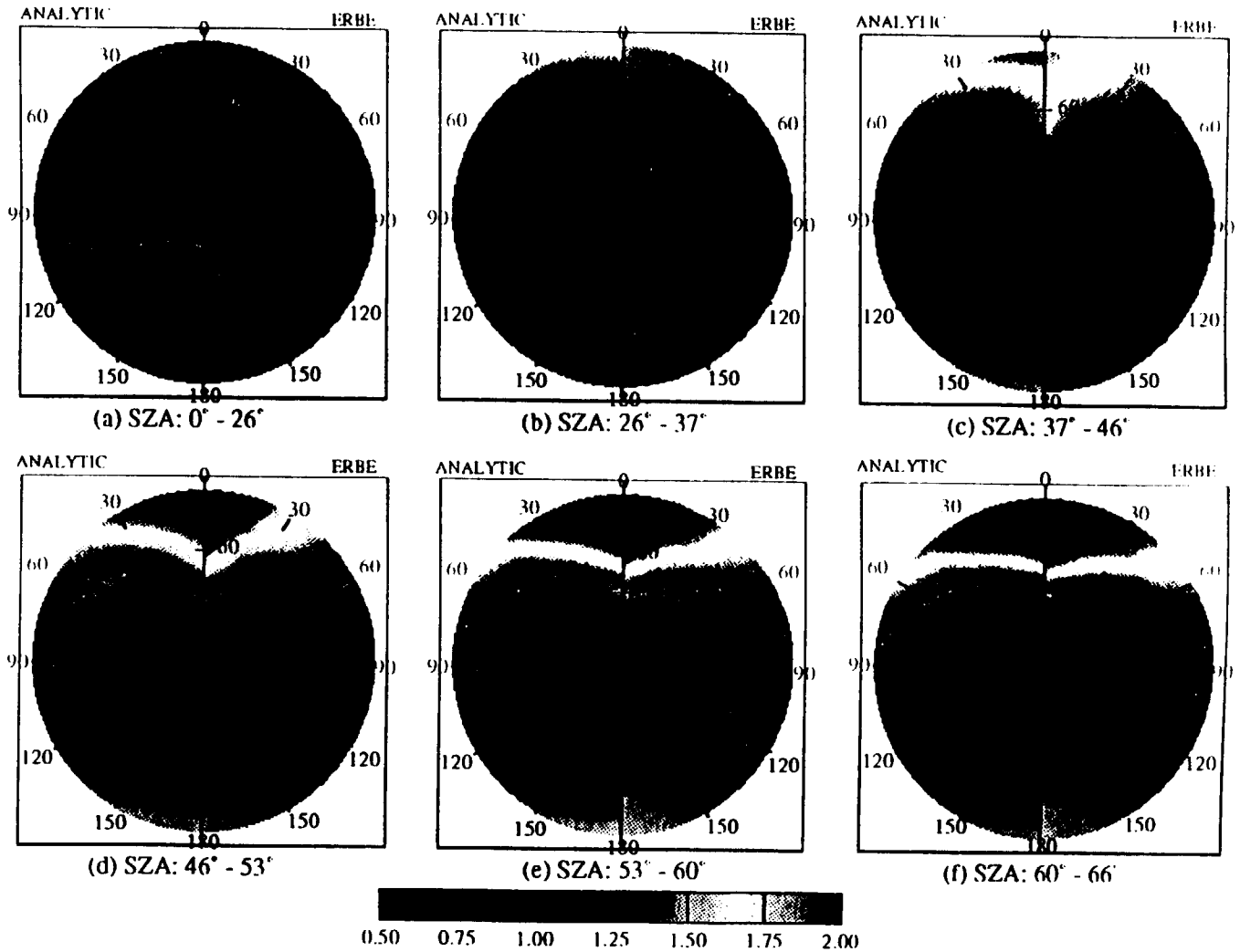

Figure 4-16. Comparison of analytic and ERBE BDRF for partly cloudy / ocean (C_1 = 0.040, C_2 = 0.047, C_3 = 0.577, C_4 = 0.008, C_5 = 1.157).

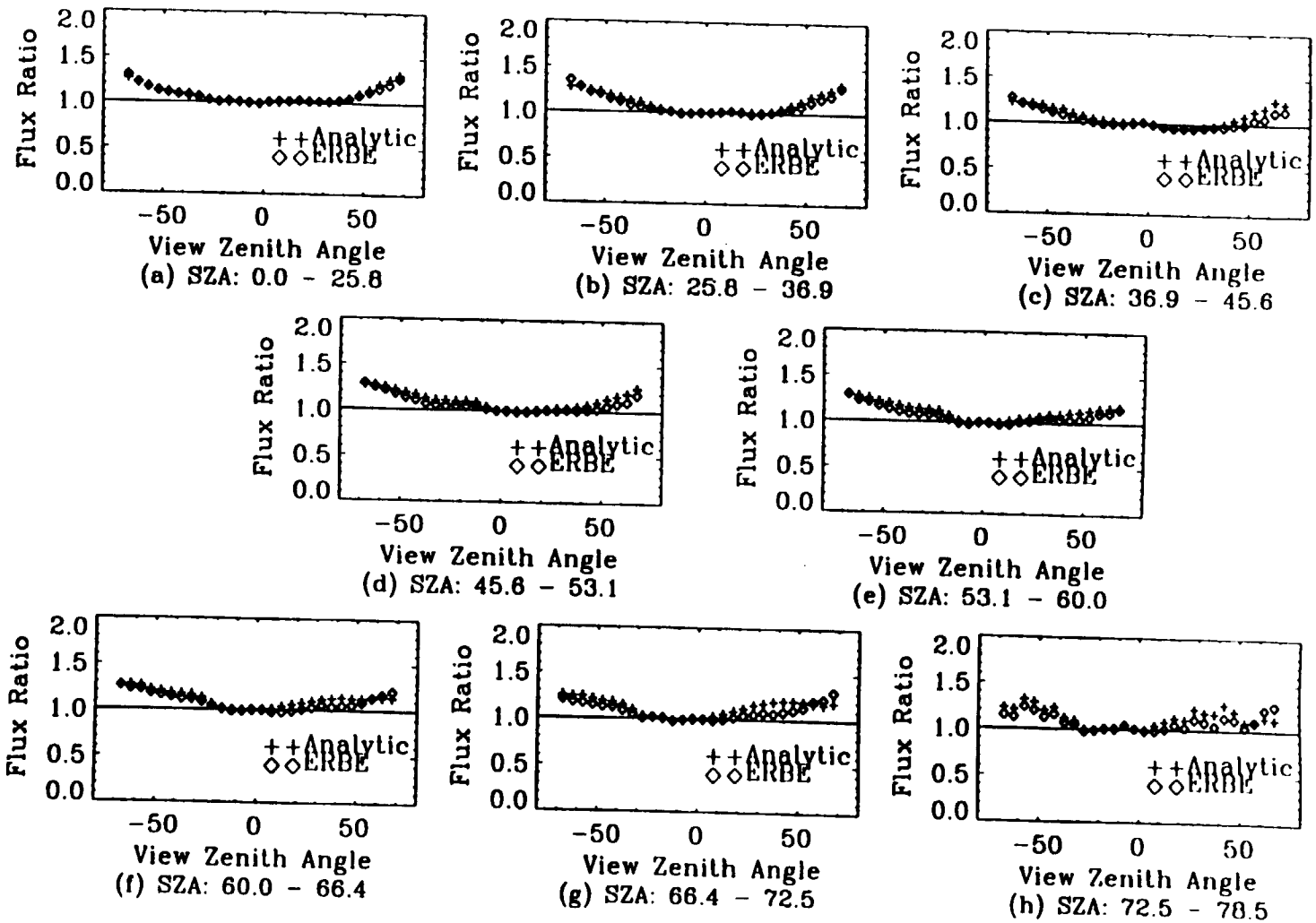

Figure 4-17. Ratio of alongtrack SW flux for partly cloudy over ocean.

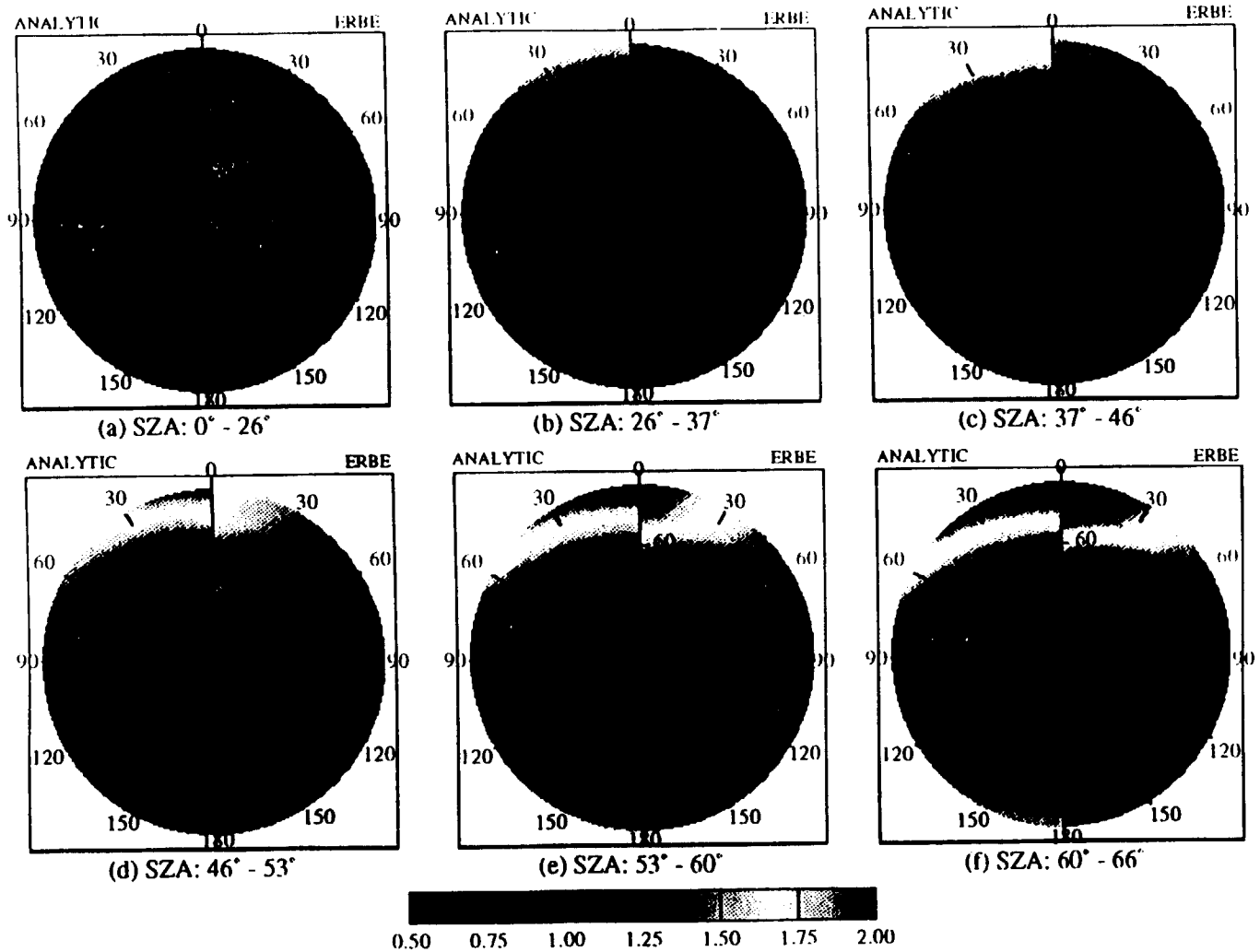

Figure 4-18. Comparison of analytic and ERBE BDRFs for MC / ocean (A = 0.025, B = 0.812, G = 0.5250, K = 0.988).

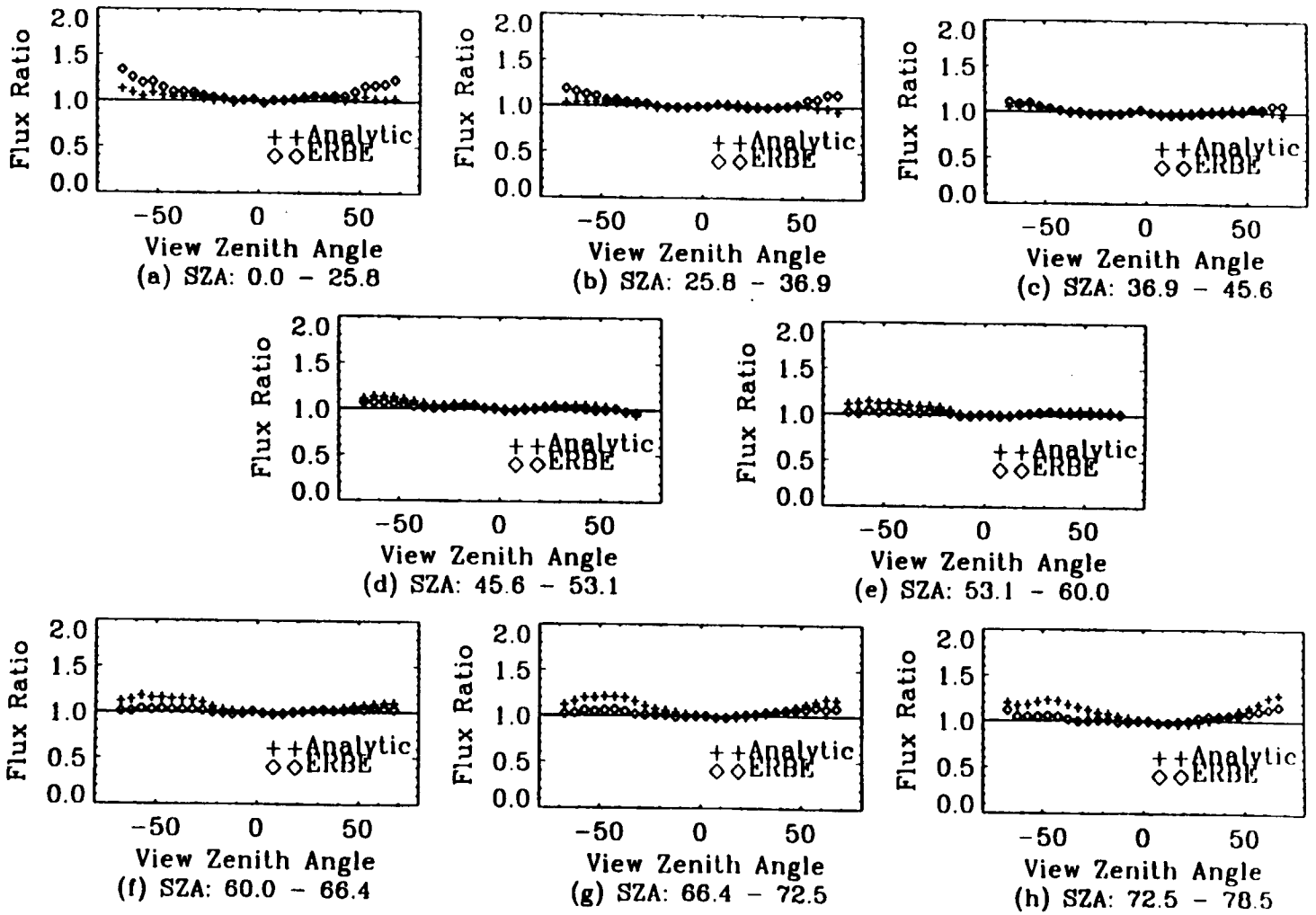

Figure 4-19. Ratio of alongtrack SW flux using the analytic and ERBE BDRF for mostly cloudy over ocean.

Chapter 5
CONCLUSIONS

In this study, an analytic expression for the bidirectional reflectance function is formulated by applying an analytic fit to the ERBE operational models. The analytic BDRF is based on theoretical considerations. The analytic BDRF is a function of viewing geometry and scene type. For each scene type, a single set of model parameters is required for application to any combination of viewing angles. The form of this expression satisfies the principle of reciprocity and is smooth in terms of the directional angles. Results are presented for four ERBE scene types namely clear ocean, partly cloudy over ocean, mostly cloudy over ocean, and overcast scenes. The analytic BDRF patterns match the ERBE operational BDRFs. The analytic functions closely modeled the reflectances in the forward scatter direction but in the backscatter direction, the analytic models were slightly more limb-brightened than the ERBE operational models.

Because these model coefficients are based upon mean radiances, the model coefficients have nominal values. However, due to the influences of variabilities in the surface and the atmosphere, the coefficients will vary. Statistical properties of the model coefficients were determined from which shortwave radiance statistics were computed and compared with the ERBE models. For clear ocean, the SWR σ were of the order +- 2 $Wm^{-2}sr^{-1}$ of the ERBE SWR σ. This difference becomes more significant in the specular region in the forward scatter direction. For overcast case, at solar zenith angles less than 46°, the largest difference in SWR σ occurs at the limb for azimuthal angles between 90° and 120°. At the specular regions in the forward scatter direction, the difference is significant especially at higher solar zenith angles.

The effectiveness of the analytic BDRF in accounting for the anisotropy at any viewing angle is evaluated with the ERBE alongtrack data. A given target area viewed from any direction must yield the same flux. The alongtrack data is ideal for validating the BDRFs since the experiment is designed to observe a single site

from multiple viewing angles. Because the ERBE clear ocean BDRF resulted in more significant flux increase from nadir to limb than the Dlhopolsky BDRF for clear ocean, the latter was used to tune the model coefficients. Although albedo growth is still evident for all models (analytic, ERBE, Dlhopolsky) studied, the tuned BDRF showed an improvement in accounting for anisotropy at the limb over the ERBE models. For other scenes presented, the flux ratio using the analytic BDRF showed some improvement and /or matched the results of the ERBE operational models, especially for solar zenith angles less than 60°.

The results of this study can be used for validation and interpretation of data from future earth radiation budget missions such as CERES.

REFERENCES

1. Smith, G. L., Green, R. N., Raschke, E., Avis, L. M., Suttles, J. T., Wielicki, B. A., and Davies, R., "Inversion Methods for Satellite Studies of the Earth's Radiation Budget: Development of Algorithms for the ERBE Mission," Reviews of Geophysics, Vol. 24, No. 2, 1986, pp. 407 - 421.
2. Raschke, E., Vonder Haar, T. H., Bandeen, W. R., and Pasternak, M., "The Annual Radiation Balance of the Earth-Atmosphere System during 1969-1970 from the Nimbus-3 Measurements," Journal of the Atmospheric Sciences, Vol. 30, No. 3, 1973, pp. 341-364.
3. Brennan, B., Halev, M., and Strange, I.,"A Radiation Climatology in the Visible and Infrared from TIROS Meteorological Satellites," NASA TN D-2534, June 1965.
4. Green, R. N., Suttles, J. T., and Wielicki, B. A., "Angular Dependence Models for Radiance to Flux Conversion, "Long-Term Monitoring of the Earth's Radiation Budget, Bruce R. Barkstrom, editor, Proceedings of SPIE 1299, Orlando, Florida, 1990, pp. 102-111.
5. Larsen, J. C., and Barkstrom, B. R., "Effects of Realistic Angular Reflection Laws for Earth's Surface upon Calculations of the Earth-Atmosphere Albedo," Proceedings of Symposium on Radiation in the Atmosphere, Garmisch-Partenkirchen, FRG, 1977.
6. Coulson, K. L., and Reynolds, D. W., "The Spectral Reflectance of Natural Surfaces," Journal of Applied Meteorology, Vol. 10, December 1971, pp. 1285 - 1295.
7. Brennan, B., and Bandeen, W. R., "Anisotropic Reflectance Characteristics of Natural Earth Surfaces," Applied Optics, Vol. 9, No. 2, 1970, pp. 405 - 412.
8. Salomonson, V., and Marlatt, W. E., "Anisotropic Solar Reflectance over White Sand, Snow and Stratus Clouds," Journal of Applied Meteorology, Vol. 7, June 1968, pp. 475 - 483.

9. Ruff, I., Koffler, R., Fritz, S., Winston, J. S., and Rao, P. K., "Angular Distribution of Solar Radiation Reflected from Clouds as Determined from TIROS IV Radiometer Measurements," Journal of the Atmospheric Sciences, Vol. 25, March 1968, pp. 323 - 332.

10. Smith, W. L., Hickey, J., Howell, H. B., Jacobowitz, H., Hilleary, D. T., and Drummond, A. J., "Nimbus-6 Earth Radiation Budget Experiment," Applied Optics, Vol. 16, No. 2, 1977, pp. 306 - 318.

11. Jacobowitz, H., Soule, H. V., Kyle, H. L., House, F. B., and the Nimbus-7 ERB Experiment Team, "The Earth Radiation Budget (ERB) Experiment: An Overview," Journal of Geophysical Research, Vol. 89, No. D4, 1984, pp. 5021 -5038.

12. Taylor, V. R., and Stowe, L. L., "Reflectance Characteristics of Uniform Earth and Cloud Surfaces Derived from NIMBUS-7 ERB," Journal of Geophysical Research, Vol. 89, No. D4, 1984, pp. 4987 - 4996.

13. Staylor, W. F., "Reflection and Emission Models for Clouds Derived from Nimbus 7 Earth Radiation Budget Scanner Measurements," Journal of Geophysical Research, Vol. 90, No. D5, 1985, pp. 8075 - 8079.

14. Staylor, W. F., and Suttles, J. T., "Reflection and Emission Models for Deserts Derived from Nimbus 7 ERB Scanner Measurements," Journal of Climate and Applied Meteorology, Vol. 25, No. 2, 1986, pp. 196-202.

15. Barkstrom, B. R., and Smith, G. L., "The Earth Radiation Budget Experiment: Science and Implementation," Reviews of Geophysics, Vol. 24, No. 2, 1986, pp. 379 - 390.

16. Suttles, J. T., Green, R. N., Minnis, P., Smith, G. L., Staylor, W. F., Wielicki, B. A., Walker, I. J., Young, D. F., Taylor, V. R., and Stowe, L. L., "Angular Radiation Models for Earth-Atmosphere System," Vol. 1, NASA Reference Publication 1184, July 1988.

17. Kopia, L., and Lee III, R. B., "Thermistor Bolometer Scanning Radiometer: Applications and Flight experience," Optical Engineering, Vol. 31, No. 1, 1992, pp. 156 - 165.

18. Smith, G. L., Manalo, N. D., and Avis, L. M., "Limb-Darkening Functions as Derived from Alongtrack Operation of the ERBE Scanning Radiometers for August 1985," NASA Reference Publication 1243, December 1990.

19. Smith, G. L., Suttles, J. T., and Manalo, N. D., "The ERBE Alongtrack Scan Experiment," Proceedings of the International Radiation Symposium, Lille, France, 1988, pp. 242 - 244,.

20. Dlhopolsky, R., and Cess, R., "Improved Angular Directional Models for Clear Sky Ocean Derived from the Earth Radiation Budget Satellite Shortwave Radiances," Journal of Geophysical Research, Vol. 98, No. D9, 1993, pp. 16713 - 16721.

21. Barkstrom, B. R., "Earth radiation budget measurements: Pre-ERBE, ERBE, and CERES," Long-Term Monitoring of the Earth's Radiation Budget, Bruce R. Barkstrom, editor, Proceedings of SPIE 1299, Orlando, Florida, 1990, pp. 52 -60.

22. Chandrasekhar, S., Radiative Transfer, Dover Publications, New York, 1960.

23. Coulson, K. L., Bouricius, G. M., and Gray, E. L., "Optical Reflection Properties of Natural Surfaces," Journal of Geophysical Research, Vol. 70, No. 18, 1965, pp. 4601 - 4611.

24. Staylor, W. F., "Site Selection and Directional Models of Deserts Used for ERBE Validation Targets," NASA Technical Paper 2540, April 1986.

25. Wielicki, B. A., and Green, R. N., "Cloud Identification for ERBE Radiative Flux Retrieval," Journal of Applied Meteorology, Vol. 28, No. 11, 1989, pp. 1133 - 1146.

26. Staylor, W. F., Personal Communication, 1992.

27. Cox, C., and Munk, W.,"Measurements of the Roughness of the Sea Surface from Photographs of the Sun's Glitter," Journal of Optical Society of America, Vol. 44, No. 11, 1954, pp. 838 - 850.

28. Green, R. N., and Smith, G. L., "Shortwave Shape Factor Inversion of the Earth Radiation Budget Observations," Journal of the Atmospheric Sciences, No. 3, 1990, pp. 390 - 402.

APPENDICES

APPENDIX A.

APPROXIMATION OF SPECULAR ALBEDO FOR CLEAR AND PARTLY CLOUDY OVER OCEAN

Figure — Page

A-1. Specular Term $A_2 = \int_0^{\pi} \frac{d\phi}{(C_5 - \cos\alpha)^2}$ vs. cos θ — 69

(a) SZA = 0°

(b) SZA = 45°

(c) SZA = 60°

A-2. Specular Term $2 R_s \cos\theta$ vs. $\cos\theta$ for $C_4 = 0.0056$ — 70

(a) SZA = 0°

(b) SZA = 45°

(c) SZA = 60°

A-3. Specular Term $2 R_s \cos\theta$ vs. $\cos\theta$ for $C_4 = 0.008$ — 71

(a) SZA = 0°

(b) SZA = 45°

(c) SZA = 60°

APPENDIX A.

APPROXIMATION OF SPECULAR ALBEDO FOR CLEAR AND PARTLY CLOUDY OVER OCEAN

The specular reflectance is expressed as

$$r_s(\theta, \phi, \varsigma) = \frac{C_4(C_5 - 1)}{(uu_0)^{1.5}(C_5 - \cos\alpha)^2} \tag{A.1}$$

where $u = \cos\theta$, $u_0 = \cos\zeta$, and α is the angle from the line of specular reflection given by $\cos\alpha = vv_0\cos\phi + uu_0$, where $v = \sin\theta$ and $v_0 = \sin\zeta$. The directional reflectance, R_s is obtained by eliminating the azimuthal dependence. R_s is defined as

$$R_s = \frac{1}{\pi}\int_0^{\pi} r_s d\phi \tag{A.2}$$

Substituting Eq. (A.1) into Eq. (A.2) gives

$$R_s = \frac{1}{\pi}A_1 A_2 \tag{A.3}$$

where $A_1 = \dfrac{C_4\left(C_5 - 1\right)}{(uu_0)^{1.5}}$ and $A_2 = \displaystyle\int_0^{\pi} \frac{d\phi}{(C_5 - \cos\alpha)^2}$.

Since A_2 is of the form

$$\int \frac{dx}{(a + b\cos x)^2} \tag{A.4}$$

where a = C_5 - uu_0 and b = -vv_0,

$$A_2 = \frac{a\pi}{(a^2 - b^2)^{1.5}} \tag{A.5}$$

Figures A-1 (a-c) depict A_2 as a function of u for three solar zenith angles, $\theta = 0^\circ$, 30°, and 60°. These curves are the same for any value of C_4 since A_2 is independent of C_4. The peak in each solar zenith case occurs where $u = u_0$. The smaller the value of C_5, the greater the area under the curve.

The specular model albedo is computed by numerically integrating Eq. (A.2) over the viewing zenith angle as

$$A(\theta_0) = 2\int_0^1 R_s u du \tag{A.6}$$

Figures A-2 (a-c) and figs. A-3 (a-c) for $C_4 = 0.0056$ and $C_4 = 0.008$, respectively, show $2R_s u$ as a function of u for varying values of C_5 for the three incident angles. As C_4 increases, the specular term increases. The peak for each case occurs at $u = u_0$. The C_5 is associated with surface roughness in the specular term. An increase in this parameter can be interpreted as an increase in wind speed and a decrease corresponds to low or calm conditions. From this figures, a low C_5 corresponds to high specular peak while a large C_5 corresponds to a broadening of the specular term.

For each solar zenith angle, albedo is computed from Eq. (A.6). D is computed as

$$D = \frac{1}{N}\Sigma A(\Theta_0) u_0^2 \tag{A.7}$$

where N = 3 (i.e. $\theta_0 = 0^\circ, 30^\circ, 60^\circ$).

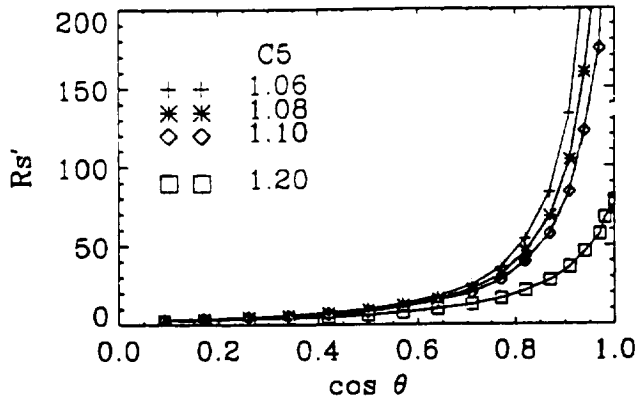

(a) SZA = 0

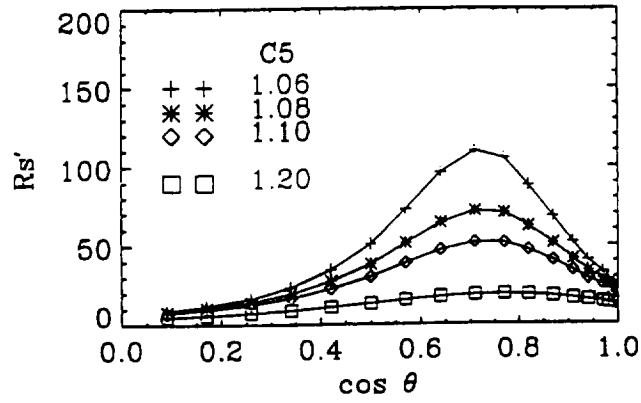

(b) SZA = 45

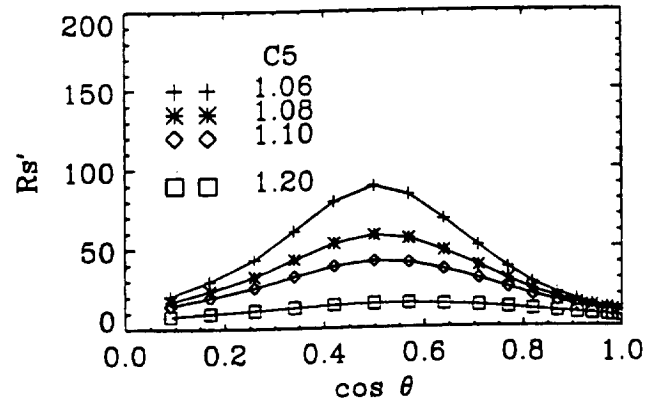

(c) SZA = 60

Figure A-1. Specular Term $A_2 = \int_0^{\pi} \frac{d\phi}{(C_5 - \cos\alpha)^2}$ vs. cos θ

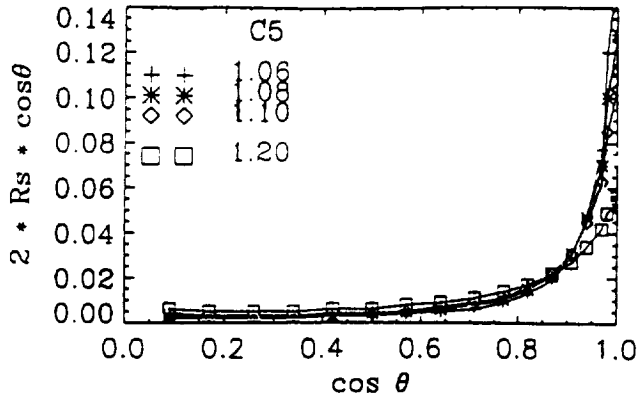

(a) SZA = 0

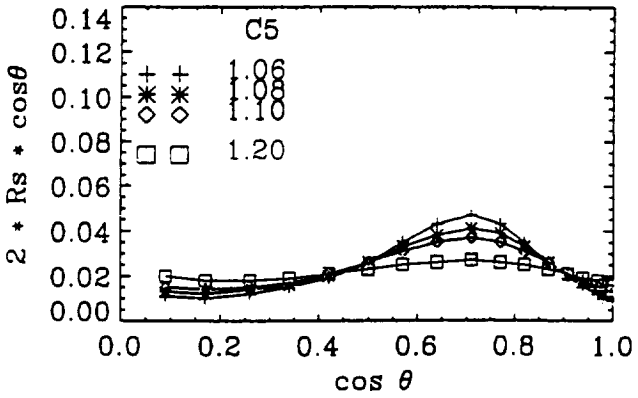

(b) SZA = 45

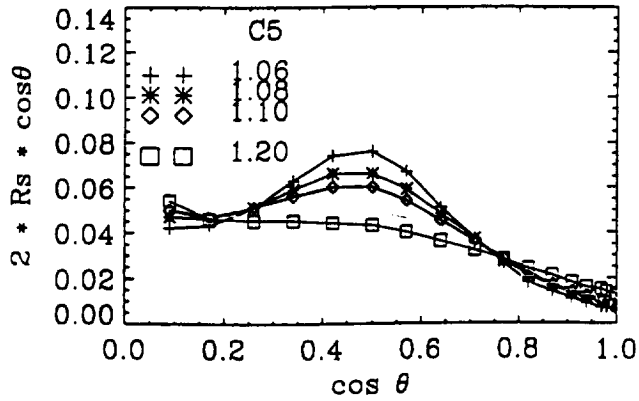

(c) SZA = 60

Figure A-2. Specular Term $2\,R_s cos\,\theta$ vs. $cos\,\theta$ for $C_4 = 0.0056$

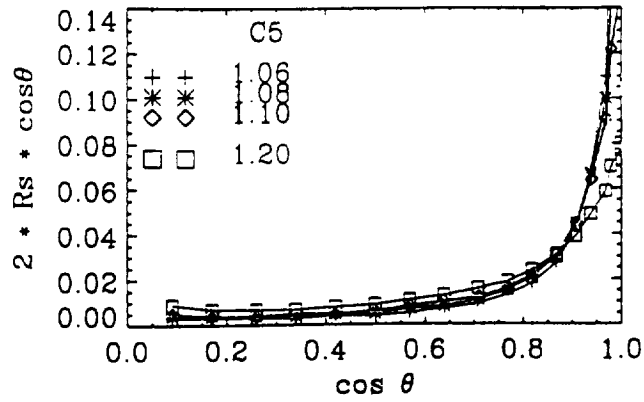

(a) SZA = 0

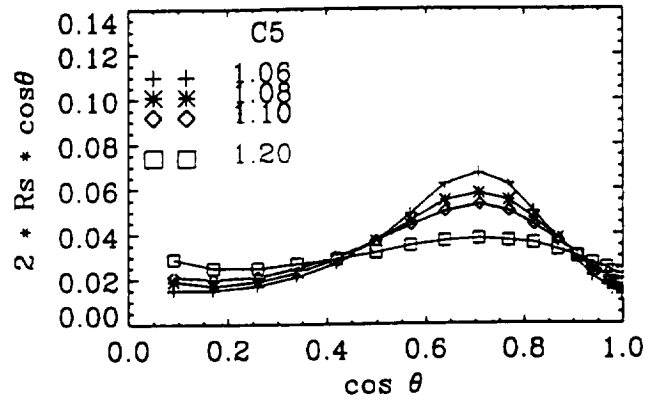

(b) SZA = 45

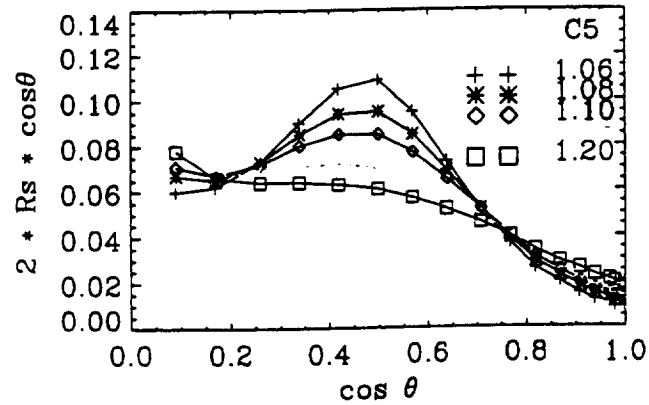

(c) SZA = 60

Figure A-3. Specular Term $2\,R_s cos\,\theta$ vs. $cos\,\theta$ for $C_4 = 0.008$

APPENDIX B.

COMPUTATION OF MODEL COEFFICIENTS FOR CLEAR AND PARTLY CLOUDY OVER OCEAN

Figure	Page
B-1. Specular Term $R_s uu_0$ vs. cos α	75

APPENDIX B.

COMPUTATION OF MODEL COEFFICIENTS FOR CLEAR AND PARTLY CLOUDY OVER OCEAN

Proposed Model:

$$r_0(\theta, \phi, \zeta) = C_1 + \frac{C_2(1 + \cos^2\gamma)}{(uu_0)^{C_3}} + \frac{C_4(C_5 - 1)}{(uu_0)^{1.5}(C_5 - \cos\alpha)^2} \qquad \text{(B.1)}$$

Data Source: ERBE operational models [14]

1. Compute bidirectional reflectances from tabulated ERBE BDRF $R_e(\theta,\phi,\zeta)$ and mean albedo $a(\zeta)$

$$r_e = R_e(\theta, \phi, \zeta)\, a(\zeta) \qquad \text{(B.2)}$$

2. Data restrictions:

   Exclude the following data -

   (a) $uu_0 < 0.1$ (non-plane-parallel)

   (b) $u_0 < 0.3$ (questionable scene type)

   (c) flagged data (insufficient sampling)

3. Reduce the specular term to a small value by editing out $\cos\alpha > 0.6$ giving the diffuse surface and atmospheric reflection terms only as

$$r_d(\theta, \phi, \zeta) = C_1 + \frac{C_2(1 + \cos^2\gamma)}{(uu_0)^{C_3}} \qquad \text{(B.3)}$$

4. Iterate on C_1 and perform linear regression of

$$\ln\frac{(R - C_1)}{1 + \cos^2\gamma} \quad \text{vs. } ln(uu_0)$$

where $R = r_e$, until the highest regression coefficient is obtained. Check for linear relationship.

5. Solve for initial values of C_1, C_2, and C_3. where

C_2 = exp(intercept)

C_3 = -slope

6. Check for the validity of the specular model. The specular reflectance is

$r_s = r_e - r_d$

Figure B-1 shows the specular reflectance term as a function of $\cos\alpha$.

7. Plot and regress $[rs(uu0)^{1.5}]^{-0.5}$ vs. $\cos\alpha$ for $\cos\alpha > 0.6$ only. Solve for

$$C_4 = \frac{-1}{slope\,(slope + intercept)} \quad \text{and} \quad C_5 = \frac{-intercept}{slope}$$

8. Recalculate $r_d(\theta, \phi, \zeta) = (r_e - r_s)$ where

$$r_s(\theta, \phi, \varsigma) = \frac{C_4(C_5 - 1)}{(uu_0)^{1.5}(C_5 - \cos\alpha)^2}$$ and recompute C_1, C_2, and C_3. by

repeating steps 4 and 5 and substituting $R = r_d$.

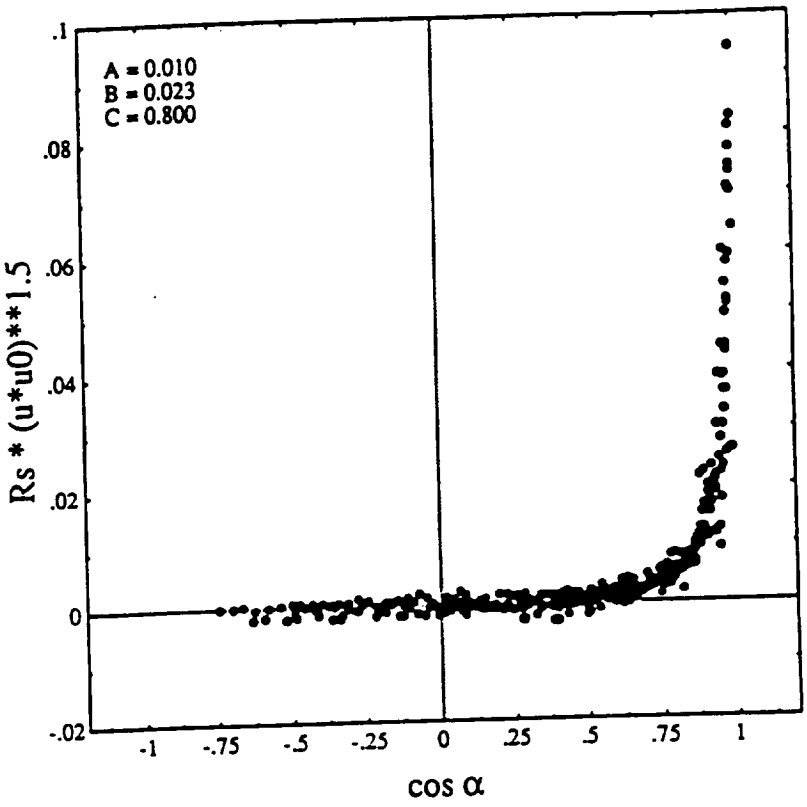

Figure B-1. Specular Term $R_s uu_0$ vs. cos α

APPENDIX C.

COMPUTATION OF MODEL COEFFICIENTS FOR LAND, SNOW, DESERT, MOSTLY CLOUDY OVER OCEAN AND OVERCAST SCENES

APPENDIX C.

COMPUTATION OF MODEL COEFFICIENTS FOR LAND, SNOW, DESERT, MC / OCEAN AND OVERCAST SCENES

Proposed Model:

$$r(model) = \omega r_{Ray} + \Psi\left[\frac{\Delta r}{\Psi}(model)\right] \tag{C.1}$$

where

$$\frac{\Delta r}{\Psi}(model) = \frac{1 + K(G + \cos\gamma)^2}{1 + K\left[G^2 - 2Guu_o + (uu_o)^2 + \frac{1}{2}(vv_o)^2\right]} \tag{C.2}$$

Data Source: ERBE operational models [10]

1. Compute bidirectional reflectances from tabulated ERBE BDRF $R_e(\theta,\phi,\zeta)$ and mean albedo $a(\zeta)$

$$r_e = R_e(\theta, \phi, \zeta)\, a(\zeta) \tag{C.3}$$

2. Data restrictions:

   Exclude the following data -

   (a) $uu_0 < 0.1$ (non-plane-parallel)

   (b) SZA restrictions:

   clear land - $u_0 < 0.3$ and $u_0 > 0.9$

   clear snow - $u_0 > 0.7$

   clear desert - $u_0 < 0.4$

   (c) flagged data (insufficient sampling)

3. Compute the azimuthally dependent reflectance by

$$\Psi = \frac{1}{\pi}\int_0^{\pi} \Delta r \, d\phi \qquad \text{(C.4)}$$

where

$$\Delta r = r_e - r_{ray} \qquad \text{(C.5)}$$

r_{ray} is the clear ocean Rayleigh reflectance term. Compute $\frac{\Delta r}{\Psi}(data)$

4. Regress $\frac{\Delta r}{\Psi}(data)$ vs. $\frac{\Delta r}{\Psi}(model)$ varying G and K until maximum regression coefficient is obtained.

5. To calculate A and B,
   Let $\Delta Y = \Psi u u_0$ and $x = u u_0 / (u+u_0)$
   Perform linear regression of ΔY and x^2. Solve for A and B from
   $\Delta Y = A + Bx^2$